






Geochemical and mineralogical classification of four new shergottites: NWA 10441, NWA 10818, NWA 11043, and NWA 12335

Kenneth J. ORR ^{1*}, Lucy V. FORMAN ¹, Kai RANKENBURG ², Noreen J. EVANS ²,
Bradley J. McDONALD², Belinda GODEL³, and Gretchen K. BENEDIX ^{1,4,5}

¹Space Science and Technology Centre, School of Earth and Planetary Science, Curtin University, GPO Box 1987, Perth, Western Australia 6845, Australia

²School of Earth and Planetary Science/John de Laeter Centre, Curtin University, GPO Box 1987, Perth, Western Australia 6845, Australia

³CSIRO Mineral Resources, ARRC, Kensington, Western Australia, Australia

⁴Department of Earth and Planetary Science, Western Australia Museum, Locked Bag 49, Welshpool, Western Australia 6986, Australia

⁵Planetary Science Institute, 1700 E. Fort Lowell, Suite 106, Tucson, Arizona 85719, USA

*Corresponding author. E-mail: kenneth.orr@postgrad.curtin.edu.au

(Received 25 August 2020; revision accepted 07 February 2022)

Abstract—Martian meteorites are rare; therefore, the discovery of new meteorites has the potential to significantly expand our current understanding of Mars. In this study, we describe four new shergottites, all found within the past 5 yr, in Northwest Africa (NWA): NWA 10441, NWA 10818, NWA 11043, and NWA 12335. To determine the geochemical and mineralogical composition of these new shergottites, a number of traditional and nontraditional analytical techniques were utilized, such as high-resolution X-ray computed tomography (for 3-D modal abundance determination) and electron backscattered diffraction (for identification of shock features). This enabled a comprehensive, nondestructive investigation of the in situ and bulk characteristics of these meteorites. From the results, we confirm the preliminary classifications of NWA 10441 and NWA 12335 as basaltic (diabasic), and NWA 10818 and NWA 11043 as poikilitic, shergottites. Chondrite-normalized rare earth element (REE) patterns of shergottites distinguish likely source reservoirs in the Martian mantle. NWA 10441 and NWA 12335 have bulk enriched REE patterns. NWA 10818 has an intermediate REE pattern, being slightly depleted in the light REE. Although published data for bulk rock REE in NWA 11043 indicate an enriched pattern, here we show that targeted in situ analyses of unaltered minerals reveal an intermediate REE pattern, suggesting that terrestrial weathering combined with shock processes experienced by these meteorites on ejection may affect the bulk analysis. Extensive fracturing in NWA 11043 likely acted as conduits for terrestrial alteration products. We suggest that in situ spot checking of REE in meteorites will constrain any weathering effect on the REE pattern of the bulk rock.

INTRODUCTION

Martian meteorites are extremely rare, comprising <0.5% (~300 paired and unpaired meteorites) of the total number of confirmed meteorites in the world (Meteoritical Bulletin Database as of January 2022). Therefore, the discovery of new meteorites from Mars represents an exciting opportunity to expand our

understanding of the only samples of the Martian surface available on Earth. Aside from NWA 7034 and its pairs, Martian meteorites are predominantly igneous and can be split into three main groups (not including the single orthopyroxenite, ALH 84001): shergottites, nakhlites, and chassignites. The nakhlites and chassignites, which are compositionally clinopyroxenites and dunites, respectively, are the least abundant groups (constituting

<15% of Martian meteorites combined). Based on geochemical similarities, cosmic ray exposure, and crystallization ages, nakhlites and chassignites are thought to be comagmatic, possibly ejected from the same source crater (McCubbin et al., 2013). Shergottites are the most common group of Martian meteorite and can be broadly classified into three subgroups based on composition, mineralogy, and texture: basaltic, olivine–phyric, and poikilitic (e.g., McSween & Treiman, 1998).

The basaltic shergottites, the largest group, are mafic rocks containing pyroxene (pigeonite and augite) and plagioclase (often shocked to form the diaplectic glass maskelynite; e.g., Bridges & Warren, 2006). According to the Mars Meteorite Compendium (<https://www-curator.jsc.nasa.gov/antmet/mmc/index.cfm>), they can be divided into textural subgroups (fine-grained, diabasic, and gabbroic) based on their varying grain size. Fine-grained and diabasic shergottites are interpreted to form in near-surface intrusive and/or surface extrusive lava flows with varying abundances of cumulate crystals in the magma (e.g., McSween & McLennan, 2013). In contrast, gabbroic shergottites, only recently characterized (<5–10 yr, e.g., Filiberto et al., 2014; Udry et al., 2017), are partially crystallized cumulates thought to have formed in the feeder hypabyssal system of the fine-grained and diabasic shergottites which erupted onto the Martian surface (e.g., Filiberto et al., 2018; Udry et al., 2017).

Olivine–phyric shergottites, similarly, are mafic rocks, but primarily comprise euhedral to subhedral olivine phenocrysts surrounded by a fine-grained basaltic groundmass (Goodrich et al., 2003). The olivine phenocrysts crystallized at depth, and subsequently, the magma followed a multistage crystallization sequence during ascension up through the Martian crust until the magma was finally shallowly emplaced or erupted onto the surface (e.g., Usui et al., 2008).

Poikilitic shergottites are ultramafic to mafic rocks that contain characteristic bimodal texture (e.g., Walton et al., 2012). Poikilitic regions in these rocks are composed of pyroxene (pigeonite core, augite rim) oikocrysts enclosing smaller olivine and chromite chadacrysts (e.g., Udry et al., 2020). Nonpoikilitic regions are composed of smaller olivine, pyroxene (pigeonite and augite), and maskelynite grains. The relative ratio of poikilitic and nonpoikilitic textures varies between the different samples of this group. Similar to the olivine–phyric shergottites, it is thought that the poikilitic shergottites started crystallizing at depth and then followed a polybaric crystallization path (Howarth et al., 2014). The poikilitic areas crystallized first and nonpoikilitic regions formed as the magma ascended and the interstitial melts accumulated and crystallized. Unlike the other shergottites, poikilitic

shergottites do not appear to have erupted onto the surface but were likely emplaced in a dike or sill near the surface (e.g., Combs et al., 2019).

The shergottites are further classified geochemically based on chondrite (CI) normalized bulk rare earth element (REE) composition. They are designated as enriched, intermediate, or depleted based on the relative abundance of light REE (LREE; La, Ce, Pr, Nd, and Sm) and heavy REE (HREE; Eu, Gd, Tb, Dy, Ho, Er, Tm, Yb, and Lu; e.g., Borg & Draper, 2003). In this case, enriched refers to a flat REE profile and depleted profiles are characterized by a lower abundance of LREE relative to HREE. The REE signature of a shergottite, and in turn, the isotope (from systems such as Rb–Sr, Sm–Nd, Lu–Hf, and Re–Os) systematics, relates directly to its magmatic source, reflecting either a heterogeneous mantle with enriched and depleted reservoirs or a homogenous depleted mantle where enrichment was caused by crustal contamination (e.g., McSween, 2015).

In this paper, we present mineralogical and geochemical data on four new Martian meteorites (all shergottites), all discovered in Northwest Africa (NWA) in the past 5 yr: NWA 10441, NWA 10818, NWA 11043, and NWA 12335 (Bouvier, Gattacceca, Agee, et al., 2017; Bouvier, Gattacceca, Grossman, et al., 2017; Gattacceca et al., 2019, 2020). We confirm the preliminary classifications of these meteorites and assess whether a suite of nondestructive analytical approaches can be used to provide comprehensive geochemical analysis while preserving the bulk of the meteoritic material.

SAMPLES AND METHODS

The Institute of Meteoritics at the University of New Mexico supplied ~0.5 g chips of each meteorite: NWA 10441, NWA 10818, NWA 11043, and NWA 12335. These chips were first scanned by high-resolution X-ray computed tomography, then cut to create both a thick section and a 1-inch epoxy mount.

NWA 10441 and 12335 were provisionally classified as basaltic shergottites in the diabasic textural subgroup (Bouvier, Gattacceca, Agee, et al., 2017; Gattacceca et al., 2020). NWA 10441 is thought to be one of the pairs of NWA 8656, which has previously been verified as an enriched basaltic shergottites (Cao et al., 2018; Howarth et al., 2018). NWA 10818 and 11043 were provisionally classified as poikilitic shergottites (Bouvier, Gattacceca, Grossman, et al., 2017; Gattacceca et al., 2019). NWA 11043 was classified as an enriched poikilitic shergottite (Rahib et al., 2019), though terrestrial weathering may have played a role in altering the CI-normalized REE profile (e.g., Crozaz et al., 2003).

High-Resolution X-Ray Computed Tomography

Before any sample preparation, the chips were scanned in 3-D using high-resolution X-ray computed tomography (HRXCT) with a Zeiss Versa XRM520 X-ray microscope fitted with a flat panel detector and installed at the Australian Resources Research Centre (ARRC), CSIRO Mineral Resources in Kensington, Western Australia. The instrument was set up to maximize phase contrast between the different rock-forming minerals. Analyses were acquired with beam conditions of 160 kV, 10 W, and a voxel size of 12 μm with a total of 1601 projections recorded over a 360° rotation. Each grayscale volume was segmented to provide statistics on pyroxene, olivine, and maskelynite using workflows similar to that described in Godel (2013) and to compute 3-D modal mineralogy.

Tescan Integrated Mineral Analyzer

Prior to quantitative analysis, all thin sections and epoxy round mounts were polished and coated with ~10 nm thick film of carbon. Samples were analyzed using a Tescan Integrated Mineral Analyzer (TIMA) in the John de Laeter Centre at Curtin University. The TIMA is a specifically designed scanning electron microscope (SEM) that semiquantitatively maps thin and thick sections in addition to grain mounts, using four energy-dispersive X-ray (EDS) detectors. This allows mineral phase, backscattered electron (BSE), and element X-ray maps to be collected simultaneously and quickly at a very small step size. The analyses were run in high-resolution mode with 3 μm step size at a 15 mm working distance. The beam current was controlled with a 70 nm spot size at 25 kV accelerating voltage. The maps were postprocessed using the TIMA-supplied software, in which phase maps of each sample were created and specific element maps extracted (Al, Ca, Cr, Fe, K, Mg, Na, P, Si, S, and Ti). These element maps were then combined into RGB images using Adobe Photoshop to inspect mineral phase relationships and distributions.

Using the combined RGB images, the modal mineralogy was determined using the pixel-counting method described in Ford et al. (2008). Briefly, the image map (Fig. 1) shows different mineral phases based on how elements combine. The phases are identified and selected, using the wand feature in Adobe Photoshop, to count the number of pixels. Each phase is checked multiple times to account for any automatic selection bias, from which a mean modal abundance and subsequent standard deviation are determined. These averages are verified visually. This allows an accurate determination of modal abundances of all

phases including variations in pyroxene compositions. We also compare the modal abundance of the major phases to the calculations derived by HRXCT.

Electron Probe Microanalyzer

Quantitative abundances of major and minor elements were acquired in situ using wavelength-dispersive analysis (WDS) spectrometry with the JEOL 8530F Plus electron probe microanalyzer (EPMA) at the Centre for Microscopy, Characterisation and Analysis in the University of Western Australia. The majority of analyses were carried out using Probe Software's Probe for EPMA software in Quant Mapping mode with a 15 kV accelerating voltage, 40 nA beam current, 40 ms pixel dwell time, and 2 \times 2 μm pixel size. Maskelynite and phosphate were acquired using spot analysis. A 10 μm defocused beam, at 15 kV and 15 nA, was used for maskelynite. The phosphate analysis was conducted using a focused beam (there were too many fractures for a defocused beam) with otherwise similar conditions to maskelynite. A combination of silicate and metal standards was analyzed with standard ZAF corrections applied. Detection limits were typically <0.01% for Al, Ca, K, Mg, and Si and <0.03% for Na, Mn, Cr, Fe, and Ti. Postprocessing was performed using Probe Software's CalcImage software, where the specific quant data were extracted from user-defined polygon areas of interest. Each map acquired data across an area of ~2.4 mm², which generated in excess of 2.5 million individual compositional analyses per map. Given this large number of analyses, totals between 98.5 and 101%, along with individual elemental abundances, were used to ensure extraction of only the target mineral during data reduction. Similar techniques were applied during line profile extraction. Data manipulation and presentation were achieved using WaveMetrics Igor Pro version 8 plotting software.

Electron Backscatter Diffraction

Electron backscatter diffraction (EBSD) requires a very finely polished surface; therefore, the epoxy mounts were polished for 4 h on a Buehler Vibromet II Polisher with 500 nm colloidal silica in a NaOH solution. They were then coated with a thin (~5 nm) layer of carbon. EBSD analyses were carried out on all epoxy mounts using a Tescan Mira3 VP-FESEM (variable pressure field emission scanning electron microscope) with an Oxford Instruments Symmetry CMOS detector at the John de Laeter Centre, Curtin University. The analyses were acquired using a 1.5–2 μm step size, at 20 mm working distance with a 20 kV accelerating voltage and 16 beam intensity. The samples were tilted to 70° from

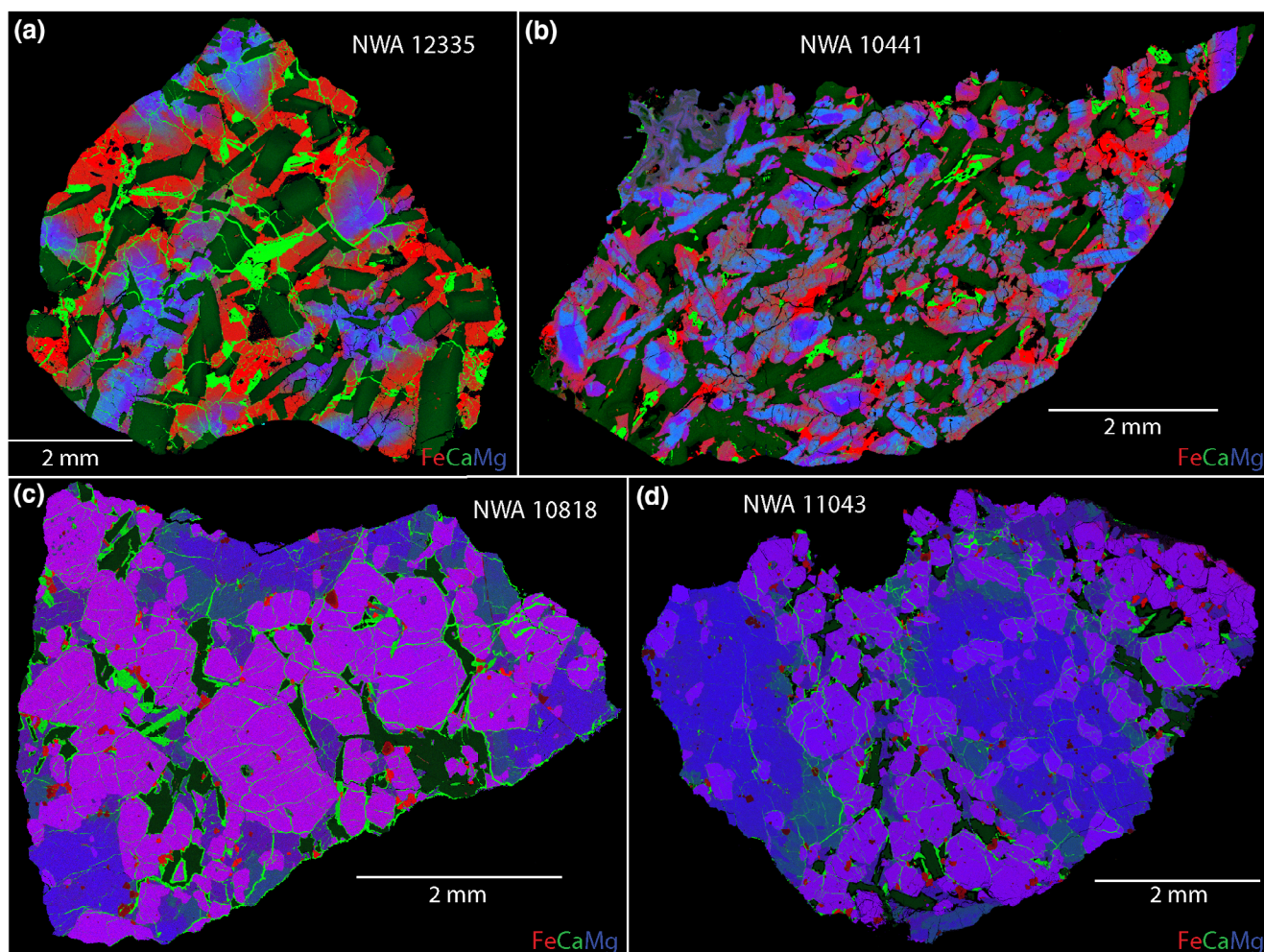


Fig. 1. Combined elemental distribution maps, Fe = red, Ca = green, and Mg = blue. a, b) The diabasic shergottites composed primarily of maskelynite (dark green) and pyroxene (red, blue, purple). c, d) The poikilitic shergottites composed primarily of olivine (purple), maskelynite (dark green), and pyroxene (blue, blue-green). Carbonate veining (bright green) is pervasive through NWA 12335, NWA 10818, and NWA 11043 but only slightly visible in NWA 10441. (Color figure can be viewed at [wileyonlinelibrary.com](https://onlinelibrary.wiley.com/doi/10.1111/ramps.13816).)

the normal position for optimum Kikuchi pattern collection. The data were gathered using the Oxford Instruments AZtec EDS/EBSD software and postprocessed using the Oxford Instruments HKL Channel 5.12 software with the Tango and Mambo modules. Noise reduction was carried out following established procedures from previous studies (e.g., Forman et al., 2019). This enabled greater grain definition (indexing) and more accurate grain determination (identification of grain boundaries) without generating significant artifacts within the data.

Laser Ablation Inductively Coupled Mass Spectrometry

In situ trace element analysis was conducted by laser ablation inductively coupled mass spectrometry (LA-ICP-MS) using a RESOLUTION-SE excimer laser and

an Agilent 8900 QQQ ICP-MS at the GeoHistory Facility, John de Laeter Centre, Curtin University. Following two cleaning pulses, analyses were conducted with a beam diameter of 50 μm with a 40 s ablation followed by 45 s of total background count rate acquisition. The laser was operated at a frequency rate of 4 Hz and a fluence of 2.7 J cm^{-2} . The primary reference material was NIST610 using ^{29}Si as the internal reference isotope for silica-bearing phases (plagioclase, olivine, pyroxene, and glass), and ^{43}Ca as the internal reference for phosphate (merrillite and chlorapatite). International reference glasses NIST612, GSD-1G, GSE-1G, BCR-2G, and BHVO-2G were interspersed with the samples and treated as secondary standards to assess accuracy. Analytical accuracy for NIST612 was better than 5% for most elements (Ti < 10%). The Iolite software package (e.g., Paton

et al., 2011) was used for data reduction. REE profiles were normalized to the optimized CI carbonaceous chondrite composition listed by Lodders and Fegley (1998).

Bulk Composition Determination

Bulk major element compositions were determined through modal reconstruction. The geochemistry of the mineralogy (as measured by EPMA) and their corresponding modal abundances were utilized to infer the bulk composition. The average compositions of each mineral and/or phase in each meteorite were combined with their respective modal abundance. The HRXCT-derived abundances were used for the major minerals. In instances where the major mineral, for example, pyroxene, has several constituent phases, the average composition of those phases at thin section-derived abundances was normalized to the HRXCT overall pyroxene abundance. Combining thin section and HRXCT modal abundances produces a more accurate bulk composition, especially for NWA 10818 and NWA 11043, where the thin section modal abundances may not be representative of the whole rock. Using this method to infer bulk major element compositions assumes that the average composition of each phase is representative of that phase within the rock (including any geochemical variation) and that all major and accessory minerals are accounted for. Capturing the geochemical variation of the mineralogy, for example, the pyroxenes in NWA 10441 and NWA 12335, is possible using EPMA quantitative mapping. Analyzing over two million points per map provides a large data set to track any geochemical variation. Additionally, using the TIMA qualitative element maps illustrates any variation for the entire sample, thus providing a representation check for the EPMA data. Associated errors propagated from modal abundance determination and geochemical variability in each phase.

RESULTS

Mineralogy, Petrology, and Geochemistry

We report results by textural grouping, first describing NWA 10818 and NWA 11043, and then NWA 10441 and NWA 12335 (Fig. 1). Broadly, NWA 10441 and NWA 12335 contain 57–67% pyroxene, 29–41% maskelynite, with the remainder composed of accessory minerals such as phosphates (3–6%), oxides (3–5.5%), and sulfides (0.6–1.2%). NWA 10818 and NWA 11043 contain 28–35% pyroxene, 7–14% maskelynite, and 52–65% olivine. A small abundance of accessory minerals are also present, such as chromites

(1–2%) and phosphates (0.6–2.1%). The modal mineralogy (Table 1) was used to infer the bulk composition of the meteorites (Table 2), based on the major element compositions of the mineralogy (e.g., Walton et al., 2012). NWA 10818 and 11043 have high Mg#s (atomic Mg/Mg+Fe) of 65.9 and 67.4, respectively. The Mg# of NWA 11043 is slightly elevated compared to NWA 10441 (Mg# 62.2) measured by Rahib et al. (2019). Much lower Mg#s were calculated for NWA 10441 and NWA 12335, at 38.5 and 23.9, respectively. NWA 10441 has a similar Mg# to its potential pair, NWA 8657 (Mg# 40.3; Howarth et al., 2018). We also compare these new meteorites with the total alkali silica (TAS) diagram, which can illustrate the similarities and differences between different sets of volcanic rocks (Fig. 2). NWA 10818 and NWA 11043 plot in the picrobasalt field, whereas NWA 10818 plots on the edge of the known shergottite field. In contrast, NWA 10441 and 12335 both plot in the basalt field, though NWA 12335 is slightly more alkaline.

Poikilitic Shergottites

NWA 10818 displays classic (in the terrestrial sense) poikilitic and nonpoikilitic textures (Fig. 1). The poikilitic regions are composed of large pyroxene ---(2–4 mm) oikocrysts surrounding smaller olivine (<1 mm) and chromite (<200 μm) chadacrysts. The nonpoikilitic regions are composed of subhedral to euhedral olivine (<1.5 mm), pyroxene (<1 mm), and anhedral maskelynite (<1 mm). Accessory phases in the nonpoikilitic regions include merrillite, chromite, ilmenite, and pyrrhotite (see Table 1 for specific modal mineralogy). Pervasive terrestrial weathering, as evidenced by carbonate veins, is also present throughout the sample. These veins have preferentially formed in the calcic-rich phases of augite and phosphates.

NWA 11043 was recently described by Rahib et al. (2019). As our results are consistent with their mineralogical and petrological findings (Table 3), we will only report on new in situ trace element compositions of the mineralogy in NWA 11043. But we include elemental maps and our modal mineralogies for completeness.

Pyroxene

The poikilitic pyroxene oikocrysts in both meteorites are chemically zoned, from pigeonite ($\text{En}_{67\pm 3.4}\text{Wo}_{8\pm 2.6}\text{Fs}_{25\pm 2.1}$) cores to augite ($\text{En}_{47\pm 3}\text{Wo}_{36\pm 3.8}\text{Fs}_{17\pm 2.8}$) rims (Table 4; Fig. 3). The pigeonite core accounts for up to ~70% of the total grain area. The augite (rim) forms a distinct boundary with the pigeonite. Nonpoikilitic pyroxene grains are also composed of pigeonite and augite with similar

Table 1. Average modal mineralogy, in percentage, of NWA 10441, NWA 12335, NWA 10818, and NWA 11043 (standard deviations are <1%). Average modal abundances of diabasic and poikilitic shergottites also shown for comparison.

Thin section point counting	NWA 10441	NWA 12335	NWA 10818	NWA 11043	Average diabasic ^a	Average poikilitic ^b
Pigeonite	26.7	10.5	19.6	32.3	52.7 ^c	26.8
Augite	24.3	11.5	9.7	10.2	–	12.5
Pyroxferroite	n.d.	19.6	n.d.	n.d.	–	–
Olivine	n.d.	n.d.	44.3	47.5	–	45.2
Maskelynite	38.0	34.6	15.1	5.7	35.5	11.7
K–Si–glass	tr.	2.4	n.d.	n.d.	–	–
Phosphates	3.3	6.1	2.1	0.6	2.2	1.1
Oxides	2.8	5.5	0.5	0.2	2	0.2
Sulfides	1.2	0.6	0.5	0.4	0.5	0.3
Chromites	0.3	0.4	1.9	0.8	–	1.2
Silica	3.4	1.5	n.d.	n.d.	1.8	–
Carbonate veins	tr.	7.2	6.3	2.3	–	–
Total	100	100	100	100	94.7	99
XCT	NWA 10441	NWA 12335	NWA 10818	NWA 11043		
Pyroxene	66.9	56.7	27.7	34.5		
Olivine	n.d.	n.d.	64.9	51.7		
Maskelynite	29.0	41.0	6.6	13.5		
Holes (vesicles)	2.2	n.d.	n.d.	n.d.		
Other	1.9	2.3	0.8	0.3		
Total	100	100	100	100		

n.d. = not detected; tr. = trace (<0.1%).

^aBarrat, Gillet, et al. (2002), Barrat, Jambon, et al. (2002), Harvey et al. (1996), Hui et al. (2011), Irving et al. (2010), Mikouchi and Barrat (2009), Roszjar et al. (2012), Rubin et al. (2000), Stöfler et al. (1986), Warren et al. (2004), Xirouchakis et al. (2002).

^bCombs et al. (2019), Howarth et al. (2014), Howarth et al. (2015), Lin et al. (2005), Rahib et al. (2019), Treiman et al. (1994), Usui et al. (2010).

^cTotal pyroxene.

Table 2. Inferred bulk major element compositions and associated errors of NWA 10818, NWA 10441, NWA 11043, and NWA 12335. Previous results for NWA 11043 and the potential pair of NWA 10441, NWA 8657, are included for comparison.

Bulk oxide wt %	Poikilitic					Basaltic				
	NWA 10818	SD	NWA 11043	SD	NWA 11043 ^c	NWA 10441	SD	NWA 12335	SD	NWA 8657 ^a
SiO ₂	40.77	1.52	42.76	1.16	41.9	49.18	2.99	48.53	1.63	50.8
TiO ₂	0.29	0.21	0.23	0.21	0.52	0.56	0.29	0.81	0.26	0.92
Al ₂ O ₃	2.43	0.64	4.26	0.70	3.05	8.20	1.44	11.13	0.79	7.55
Cr ₂ O ₃	0.43	0.86	0.28	0.42	0.97	0.13	0.15	0.04	0.07	–
MgO	25.99	1.54	24.07	1.14	22.8	6.65	2.28	3.51	1.27	7.5
FeO	23.95	1.76	20.72	1.31	24.6	18.97	3.87	19.93	2.99	19.7
MnO	0.60	0.48	0.49	0.25	0.5	0.54	0.44	0.50	0.29	0.51
CaO	3.82	0.66	5.05	0.73	4.75	11.64	1.72	10.45	2.23	10.9
Na ₂ O	0.51	0.20	0.90	0.21	0.22	1.77	0.43	2.47	0.39	1.46
K ₂ O	0.07	0.10	0.07	0.06	0.1	0.17	0.14	0.14	0.13	0.17
P ₂ O ₅	0.47	0.02	0.48	0.01	0.58	0.98	0.01	0.91	0.01	0.53
Total	99.33		99.30		100	98.79		98.42		100
Mg#	65.91		67.44		62.2	38.46		23.90		40.3

^aRahib et al. (2019).

^bHowarth et al. (2018).

sharp transitions. In contrast, zoning in the nonpoikilitic pyroxene is more interstitial with no obvious core and rim relationship. Nonpoikilitic

pigeonite and augite have compositions of $En_{60\pm 3.1}Wo_{11\pm 3.6}Fs_{29\pm 2.6}$ and $En_{45\pm 3}Wo_{37\pm 4.7}Fs_{18\pm 2.9}$, respectively, and, although within error, there is a slight

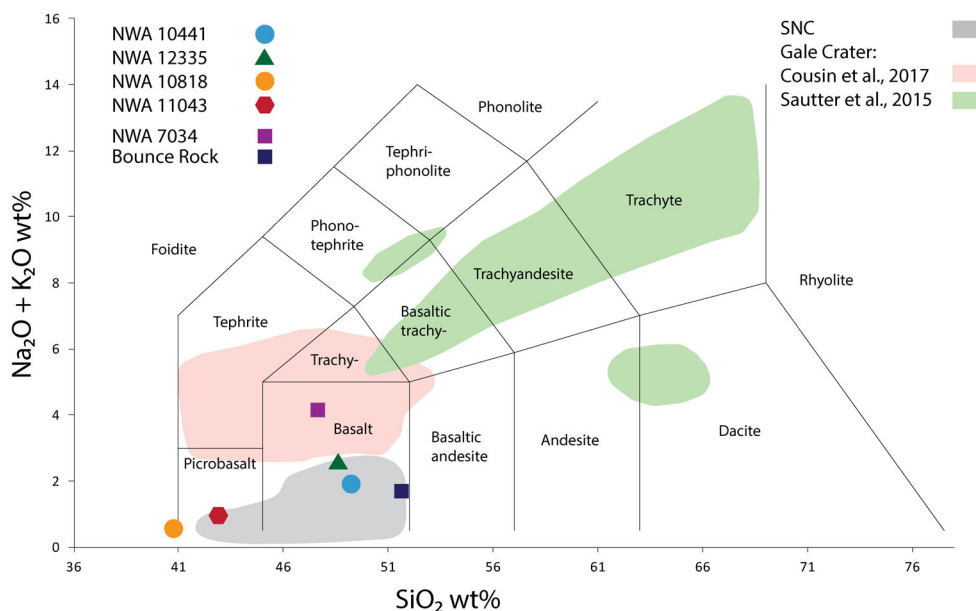


Fig. 2. Total alkali silica classification of the new shergottites compared to other Martian igneous rocks for reference: SNC (gray), NWA 7034 (a volcanic-derived polymict regolith breccia; Agee et al., 2013) Gale Crater float rocks (red: Cousin et al., 2017; green: Sautter et al., 2015), Bounce Rock (Meridiani igneous sample; Zipfel et al., 2011). Figure modified from McSween (2015). (Color figure can be viewed at wileyonlinelibrary.com.)

trend to more Fs-rich compositions. The Mg# of poikilitic pigeonite (72.6 ± 2.4) and augite (73.7 ± 3.5) is higher than that of the nonpoikilitic pigeonite (68 ± 2.5) and augite (71.7 ± 3.1), with the larger difference shown in pigeonite. The average Ti/Al ratio for both augite and pigeonite in NWA 10818 is 0.14, while in NWA 11043, the Ti/Al ratio of pigeonite and augite is 0.14 and 0.13, respectively.

All analyzed pyroxenes in NWA 10818 display a depletion in LREE (Table 5; Fig. 4). Augites, in both textures, are slightly more enriched, having $[La/Lu]_{CI}$ of 0.033 and 0.039, respectively, than pigeonite ($[La/Lu]_{CI}$ of 0.004 and 0.008, respectively). Nonpoikilitic pigeonite is more enriched in LREE than the poikilitic pigeonite whereas REE patterns for both forms of augite overlap within uncertainty (Fig. 4). Overall, pigeonite displays a positive Eu anomaly ($[Eu/Eu^* = Eu_{CI}/(Sm_{CI} * Gd_{CI})^{1/2}] = >1$) compared to augite, which displays a negative Eu anomaly ($Eu/Eu^* = <1$). Average REE concentrations in NWA 10818 pyroxenes are ~ 0.1 times CI in the LREE and ~ 4 times CI in the HREE (Fig. 5).

Pyroxenes in NWA 11043 behave similarly to those in NWA 10818 and average REE concentrations are ~ 0.4 times CI for LREE and four times CI for HREE (Table 6). The poikilitic pigeonite is least abundant in REE with poikilitic augite and nonpoikilitic pigeonite having similar, but slightly higher abundances. Nonpoikilitic augite has the highest abundance of REE (Fig. 4). With the exception of the poikilitic augite, pyroxene shows an enrichment in La and a depletion in

Ce. This LREE pattern was similarly reported in the bulk composition of NWA 11043 (Rahib et al., 2019). The pyroxene grains also display similar Eu anomalies as those in NWA 10818, with pigeonite having a slightly positive ($Eu/Eu^* = >1$) and augite having a slightly negative ($Eu/Eu^* = <1$) Eu anomaly.

Olivine

The poikilitic olivine chadacrysts are anhedral with small inclusions of chromite ($<50 \mu m$) and basaltic melt ($<100 \mu m$), while nonpoikilitic olivine is euhedral to subhedral with similar size chromite and basaltic melt inclusions. The average forsterite content of poikilitic olivine ($Fo_{66 \pm 2.3}$) is higher than that of nonpoikilitic olivine ($Fo_{60 \pm 2.4}$) (Fig. 3). No chemical zoning is observed in any olivine grain.

Although olivine is not a major host of REE, abundances determined in this study are generally above the limit of detection (LOD). In NWA 10818, olivine in both textures shows a depleted LREE pattern with an $[La/Lu]_{CI}$ of 0.142 and 0.006, respectively, and poikilitic grains more enriched than nonpoikilitic (Fig. 6). In NWA 11043, nonpoikilitic olivine shows a relative enrichment of LREE compared to poikilitic olivine, $[La/Lu]_{CI} = 1.3$ and 1.087, respectively. Both poikilitic and nonpoikilitic olivine in NWA 10818 and NWA 11043 have a positive Eu anomaly. Due to the low abundance of REE ($<1_{CI}$) in NWA 10818, some LREE were below the detection limit for nonpoikilitic olivine.

Table 3. Representative major element compositions of the mineralogy in NWA 11043.

NWA 11043 Oxide wt%	Poikilitic		Nonpoikilitic		Poikilitic		Nonpoikilitic		Poikilitic		Nonpoikilitic	
	Pigeonite core	Augite rim	Pigeonite	Augite	Olivine	Maskelynite	Merrillite	Chromite	Chromite	Chromite	Ilmenite	
SiO ₂	52.09	50.36	50.73	49.56	35.93	53.65	1.39	2.5	2.64	1.32		
TiO ₂	0.19	0.33	0.54	0.73	0.09	0.08	—	3.14	9.64	51.29		
Al ₂ O ₃	0.88	1.65	1.38	1.97	0.2	27.22	0.7	8.16	6.88	0.55		
Cr ₂ O ₃	0.45	0.73	0.39	0.59	0.1	0.01	—	47.88	34.39	1.12		
MgO	24.36	17.61	21.24	16.24	33.76	0.14	3.46	5.55	4.65	4.66		
FeO	15.95	10.39	17.63	10.85	28.54	0.62	1.03	31.01	39.99	38.89		
MnO	0.55	0.41	0.61	0.42	0.57	0.01	0.18	0.54	0.59	0.73		
CaO	4.8	17.64	6.63	18.52	0.27	11.14	44.88	0.47	0.36	0.67		
Na ₂ O	0.24	0.55	0.37	0.78	0.11	5.09	1.73	0.21	0.31	0.23		
K ₂ O	0.05	0.04	0.05	0.05	0.03	0.24	—	0.06	0.09	0.06		
P ₂ O ₅	—	—	—	—	—	—	43.76	—	—	—		
Total	99.56	99.71	99.55	99.71	99.61	98.2	97.13	99.51	99.56	99.52		
Fo					66.13							
An						53.95						
Ab						44.65						
Or						1.4						
Wo	9.39	35.1	13.27	37.35								
En	66.27	48.76	59.17	45.57								
Fs	24.34	16.14	27.55	17.08								

Table 4. Representative major element compositions of the mineralogy in NWA 10818.

NWA 10818 Oxide wt%	Poikilitic		Nonpoikilitic		Poikilitic		Nonpoikilitic		Poikilitic		Nonpoikilitic	
	Pigeonite core	Augite rim	Pigeonite	Augite	Olivine	Nonpoikilitic	Maskelynite	Merrillite	Chromite	Chromite	Chromite	Ilmenite
SiO ₂	52.73	51.77	51.48	49.92	35.91	36.29	53.94	2.08	3.54	1.22	1.69	1.69
TiO ₂	0.19	0.42	0.5	0.74	0.1	0.09	0.08	–	1.76	13.64	52.89	52.89
Al ₂ O ₃	0.85	1.86	1.2	1.94	0.31	0.39	27.3	1.3	7.39	6	0.45	0.45
Cr ₂ O ₃	0.44	0.77	0.33	0.61	0.19	0.09	0.01	–	50.55	28.12	1.12	1.12
MgO	24.23	16.28	21.1	15.99	33.88	29.15	0.14	3.51	5.73	4.22	4.38	4.38
FeO	16.22	10.41	18.29	11.32	28.18	32.32	0.58	1.12	28.92	44.99	37.79	37.79
MnO	0.59	0.52	0.68	0.47	0.54	0.8	0.01	0.36	0.55	0.66	0.82	0.82
CaO	3.99	17.18	5.64	17.88	0.27	0.32	11.08	44.35	0.74	0.38	0.33	0.33
Na ₂ O	0.2	0.38	0.27	0.66	0.11	0.11	4.99	1.66	0.22	0.19	0.16	0.16
K ₂ O	0.08	0.07	0.06	0.05	0.05	0.07	0.25	–	0.08	0.05	0.07	0.07
P ₂ O ₅	–	–	–	–	–	–	–	42.65	–	–	–	–
Total	99.52	99.66	99.54	99.6	99.53	99.62	98.38	97.04	99.49	99.46	99.71	99.71
Fo					67.47	60.76						
An							54.33					
Ab							44.22					
Or							1.44					
Wo	7.97	35.81	11.46	36.5								
En	66.88	47.24	59.55	45.44								
Fs	25.15	16.95	28.99	18.07								

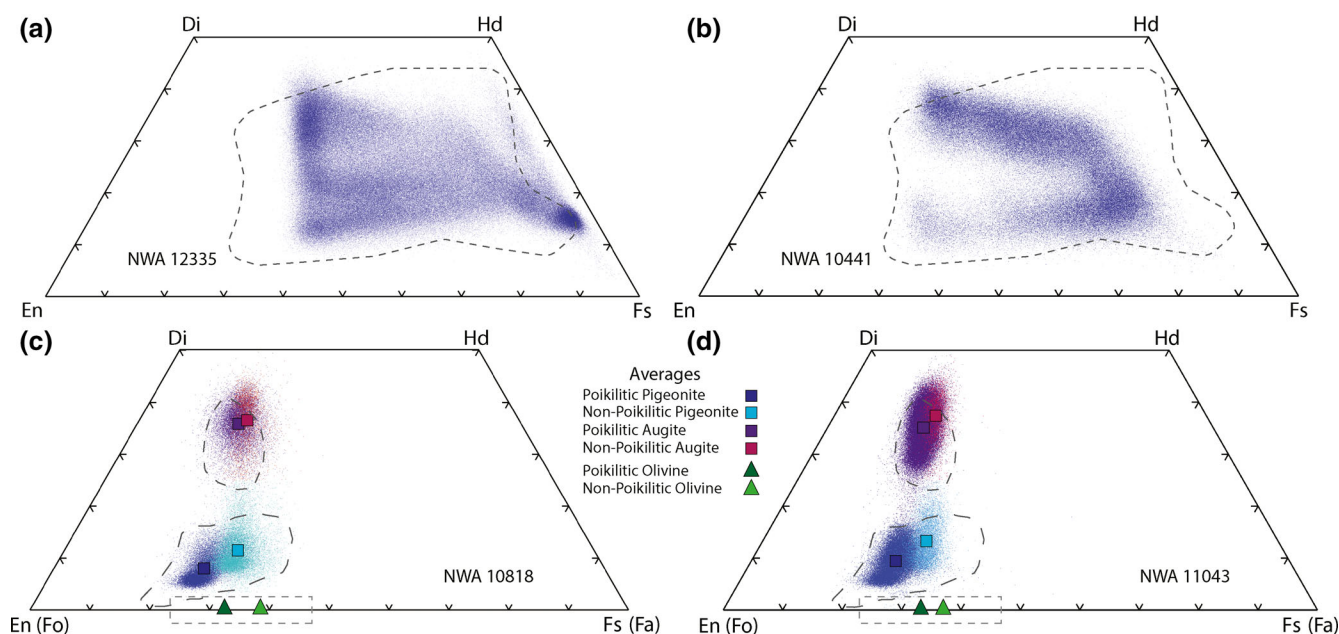


Fig. 3. Pyroxene quadrangle (Di = diopside, Hd = hedenbergite, En = enstatite, Fs = ferrosilite). Pyroxene and olivine compositions of (a) NWA 12335, (b) NWA 10441, (c) NWA 10818, and (d) NWA 11043. Note the difference in compositional range between the diabasic (a and b) and poikilitic shergottite (c and d) pyroxenes. The gray-dashed lines represent pyroxene compositions from other basaltic (Filiberto et al. [2018] and references therein) and poikilitic (Rahib et al. [2019] and references therein) shergottites. Light gray dashed lines represent olivine compositions from other poikilitic shergottites (e.g., Kizovski et al., 2019; Rahib et al., 2019). (Color figure can be viewed at wileyonlinelibrary.com.)

Table 5. Representative REE abundance (ppm) in minerals from NWA 10818, n equals the number of analyses averaged.

NWA 10818	Poikilitic	Nonpoikilitic	Poikilitic		Nonpoikilitic		Nonpoikilitic	
	Olivine		Pigeonite core	Augite rim	Pigeonite	Augite	Phosphate	Maskelynite
n	5	17	11	7	8	5	9	10
La	0.017	0.001	0.001	0.031	0.007	0.040	32.349	0.115
Ce	0.064	0.011	0.010	0.177	0.058	0.214	81.349	0.245
Pr	0.003	b.d.	0.001	0.038	0.009	0.046	12.697	0.029
Nd	0.022	b.d.	0.012	0.334	0.077	0.422	76.601	0.160
Sm	0.004	b.d.	0.016	0.376	0.119	0.417	45.404	0.067
Eu	0.032	0.010	0.015	0.163	0.078	0.179	16.462	0.683
Gd	0.016	0.002	0.062	0.930	0.369	1.085	85.011	0.101
Tb	0.003	0.001	0.016	0.199	0.090	0.228	15.384	0.021
Dy	0.030	0.020	0.155	1.508	0.789	1.713	103.348	0.166
Ho	0.008	0.006	0.036	0.316	0.187	0.363	20.664	0.029
Er	0.035	0.030	0.128	0.878	0.578	0.971	55.684	0.114
Tm	0.006	0.006	0.019	0.115	0.085	0.128	7.187	0.012
Yb	0.065	0.072	0.137	0.715	0.612	0.791	43.358	0.070
Lu	0.012	0.015	0.022	0.101	0.097	0.109	5.908	0.010

b.d. = below detection limit.

Maskelynite

In both meteorites, plagioclase has been fully converted to maskelynite glass due to impact-related shock processes. The maskelynite morphology (based on the original plagioclase shape) is generally anhedral,

only partially retaining the plagioclase lath crystal structure, with grains up to 1 mm long. Maskelynite occurs exclusively in nonpoikilitic regions, though some maskelynite occurs on the rims of the pyroxene oikocrysts. The average composition of maskelynite in

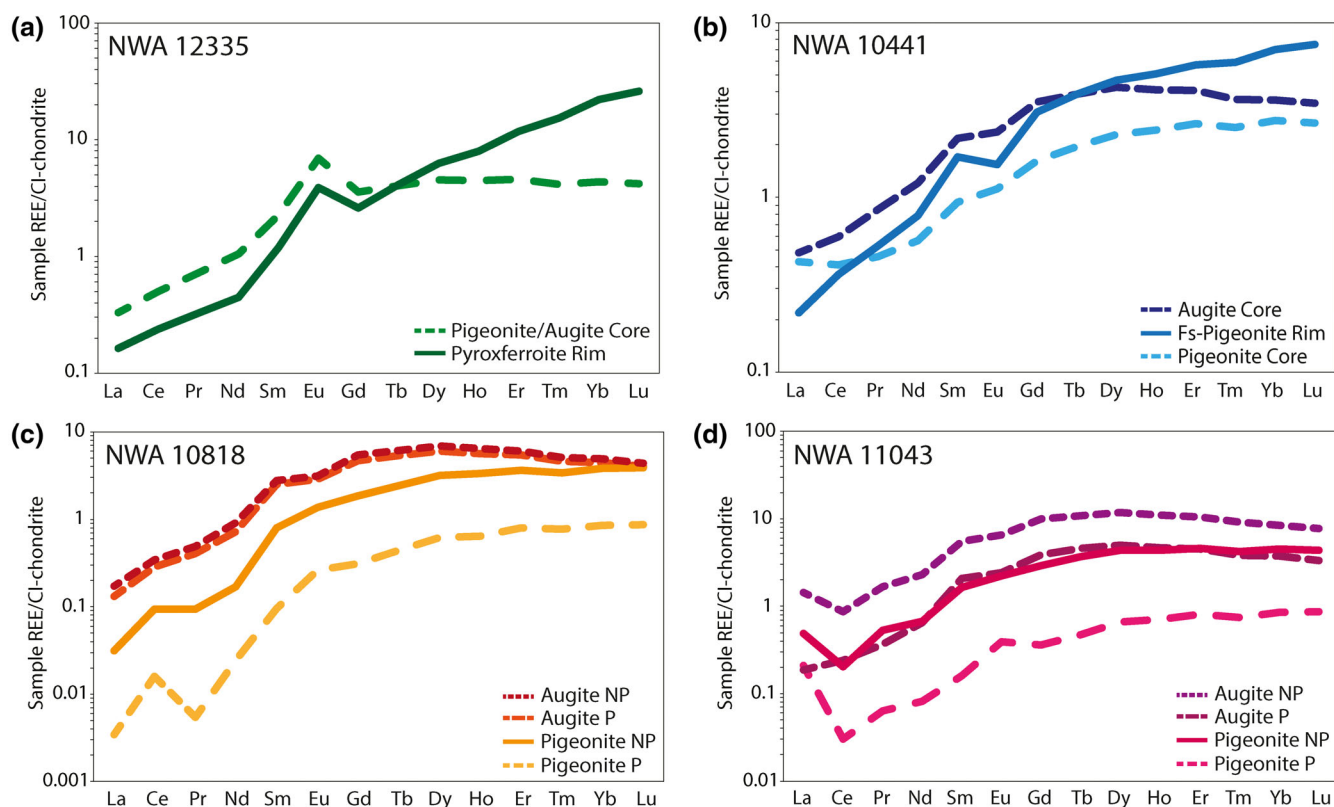


Fig. 4. Chondrite-normalized pyroxene REE profiles from augite and pigeonite zones. a, b) Diabasic shergottites average pigeonite, augite, and pyroxferroite rim REE profiles. Note due to the complexity of pigeonite and augite zoning in NWA 12335, the average of both has been shown. c, d) The poikilitic shergottites showing pigeonite and augite REE distribution in poikilitic (P) and nonpoikilitic (NP) areas. (Color figure can be viewed at wileyonlinelibrary.com.)

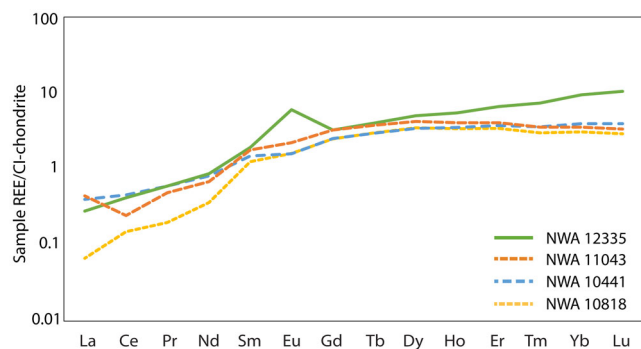


Fig. 5. Chondrite-normalized average REE profiles based on thin section modal abundances of all the pyroxenes in NWA 10441, NWA 10818, NWA 11043, and NWA 12335. This is the weighted average used in the bulk REE calculations. (Color figure can be viewed at wileyonlinelibrary.com.)

NWA 10818 is $An_{50.7 \pm 7.3}Ab_{47.3 \pm 7.1}Or_{1.9 \pm 0.9}$, which just fits into the labradorite field, though with some variation into andesine.

The REE pattern of maskelynite shows that it is relatively enriched in the LREE with an $[La/Lu]_{CI}$ of 1.22 for NWA 10818 (Fig. 6). In NWA 11043, HREE

(Tm-Lu) abundances were below LOD. Maskelynite in both NWA 10818 and NWA 11043 exhibits a positive Eu anomaly ($Eu/Eu^* = 25.19$ and 123.93 , respectively), with the anomaly being an order of magnitude larger in NWA 11043.

Chromite

Chromite grains in NWA 10818 are generally anhedral to subhedral and $<200 \mu m$ in size. They are observed in both poikilitic and nonpoikilitic areas. In thin section, the poikilitic chromite grains can be inclusions in olivine chadacrysts, or form chadacrysts themselves, enclosed by the larger pyroxene oikocrysts. In nonpoikilitic areas, chromite exists as inclusions in pyroxene and olivine, but also as distinct grains interstitial to pyroxene and olivine. Poikilitic chromite has higher average Mg# and Cr# (atomic $Cr/Cr+Al$) than nonpoikilitic chromite (Mg# 22.8 ± 3.5 and Cr# 82.9 ± 3.3 versus Mg# 12.8 ± 2.8 and Cr# 75.7 ± 5.2 , respectively). Some of the nonpoikilitic chromite is zoned, with high Cr_2O_3 and low TiO_2 cores and the opposite trend in rims. Compositionally, the poikilitic chromite is spinel (Spn) $_{15.3 \pm 2.7}$ chromite (Chr) $_{74.6 \pm 5.7}$ ulvöspinel (Ulv) $_{4.9 \pm 3.2}$ magnetite (Mag) $_{5.2 \pm 3.3}$, while

Table 6. Representative REE abundance (ppm) in minerals from NWA 11043, *n* equals the number of analyses averaged.

NWA 11043 <i>n</i>	Poikilitic	Nonpoikilitic	Poikilitic		Nonpoikilitic		Nonpoikilitic	
	Olivine		Pigeonite core	Augite rim	Pigeonite	Augite	Phosphate	Maskelynite
	13	18	15	11	11	6	11	11
La	0.115	0.202	0.050	0.044	0.114	0.336	46.456	0.061
Ce	0.081	0.086	0.019	0.148	0.125	0.538	97.443	0.112
Pr	0.009	0.059	0.006	0.034	0.050	0.158	16.656	0.012
Nd	0.042	0.231	0.037	0.298	0.307	1.061	97.634	0.060
Sm	0.006	0.057	0.024	0.311	0.245	0.834	55.730	0.011
Eu	0.030	0.040	0.022	0.137	0.127	0.372	20.525	0.565
Gd	0.019	0.074	0.072	0.781	0.583	2.003	102.411	0.019
Tb	0.002	0.011	0.018	0.170	0.136	0.398	18.516	0.002
Dy	0.024	0.071	0.165	1.246	1.086	2.935	123.389	0.013
Ho	0.007	0.016	0.040	0.261	0.244	0.618	24.546	0.001
Er	0.030	0.055	0.129	0.721	0.733	1.685	66.258	0.001
Tm	0.006	0.009	0.019	0.095	0.105	0.228	8.490	b.d.
Yb	0.051	0.083	0.135	0.597	0.726	1.341	50.901	b.d.
Lu	0.011	0.017	0.022	0.083	0.110	0.194	6.884	b.d.

b.d. = below detection limit.

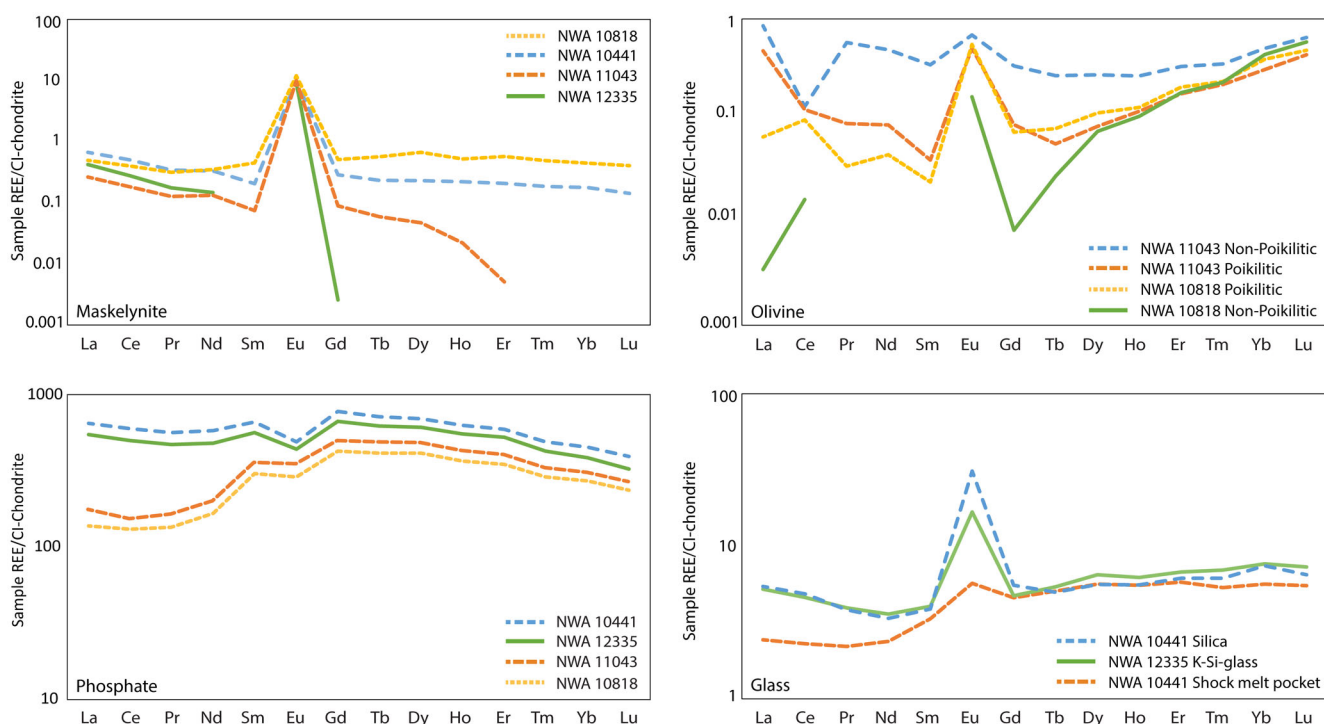


Fig. 6. Chondrite-normalized REE profiles of maskelynite, olivine, phosphate, and glass in NWA 10818, NWA 10441, NWA 11043, and NWA 12335. Olivine is only present in NWA 10818 and NWA 11043. Both poikilitic and nonpoikilitic olivine are displayed. Missing REE data are due to those analyses being below the detection limit of the instrument. (Color figure can be viewed at wileyonlinelibrary.com.)

nonzoned nonpoikilitic chromite is $\text{Spn}_{12.3 \pm 2.4} \text{Chr}_{39.8 \pm 10.2} \text{Ulv}_{36.6 \pm 10.2} \text{Mag}_{11.4 \pm 5}$ and zoned nonpoikilitic chromite is $\text{Spn}_{11.2 \pm 2} \text{Chr}_{58.6 \pm 14.6} \text{Ulv}_{24.1 \pm 13.1} \text{Mag}_{6 \pm 4.9}$. The poikilitic

grains have a much tighter compositional range than the nonpoikilitic chromites, trending to ulvöspinel compositions.

Phosphates

In NWA 10818, phosphate grains (merrillite) are anhedral and can be up to 500 μm long. The majority of the grains are observed in nonpoikilitic areas, with <5% occurring as inclusions in olivine or pyroxene. Some phosphate grains are found in poikilitic areas, generally toward the rims of the pyroxene oikocrysts or as inclusions in olivine chadacrysts.

In both NWA 10818 and 11043, phosphates are the major host phase of REE, with abundances that are >100 times those in CI. The REE profiles of merrillite in NWA 10818 and NWA 11043 are very similar (Fig. 6). Both show a relative depletion in LREE with an $[\text{La}/\text{Lu}]_{\text{CI}}$ of 0.582 and 0.66, respectively. However, similar to REE profiles in other minerals from NWA 11043, there is an enrichment in La and slight depletion in Ce. There is also a slight negative Eu anomaly $[\text{Eu}/\text{Eu}^*]$ of ~ 0.8 in NWA 10818 and NWA 11043. In NWA 11043, there is variation among the phosphate analyses with two analyses displaying a relative LREE enrichment compared to the others, as discussed below.

Accessory Phases

In NWA 10818 and NWA 11043, ilmenite is observed as subhedral to anhedral grains, <200 μm in diameter, and occurs in nonpoikilitic areas. It contains 52.9 ± 7.4 wt% TiO_2 and 37.8 ± 4 wt% FeO . Pyrrhotite is also found in nonpoikilitic regions, as anhedral grains that are <100 μm . Both ilmenite and pyrrhotite occur as inclusions in pyroxene and olivine, and also as distinct grains embedded in the matrix.

Diabasic Shergottites

NWA 10441 and 12335 are both coarse-grained with maskelynite and pyroxene (the major mineralogy) grain sizes of 1–5 and 2–3 mm, respectively. They are both of basaltic composition, composed primarily of pyroxene and similar to the poikilitic shergottites discussed above, all the plagioclase has been converted to maskelynite (see Table 1 for modal abundances). Accessory minerals include phosphate (chlorapatite and merrillite), ilmenite, magnetite, and chromite. Both samples contain silica, with NWA 12335 containing K–Si–glass, similar to that found in Los Angeles (Warren et al., 2004). As with NWA 10818 and NWA 11043, NWA 12335 also contains carbonate veins most likely emplaced during terrestrial weathering.

Pyroxene

The pyroxene grains are texturally different in both samples. In NWA 10441, the pyroxene can be extremely elongate with length:width (L:W) ratios of up to 50:4, while in NWA 12335, the pyroxene is

more anhedral. There is significant zoning (in Ca, Mg, and Fe) in pyroxene from both samples. In NWA 12335, the zoning is complex (Fig. 7), but there is a general trend from high-Mg cores (pigeonite and/or augite) to high-Fe rims (pyroxferroite in the case of NWA 12335). Augite (high-Ca pyroxene) and pigeonite (low-Ca pyroxene) occur interstitially throughout the grains (Fig. 8). In NWA 10441, the zoning is much more distinct having both augite and pigeonite cores, with a similar trend from high-Mg in the cores to high-Fe in the rims. Extensive exsolution lamellae (<1 to 8 μm) are observed between the augite and pigeonite in both meteorites (Fig. 9). In NWA 10441, pigeonite has an average composition of $\text{En}_{27.8 \pm 10.1} \text{Wo}_{17.2 \pm 3.6} \text{Fs}_{55.1 \pm 9}$ while augite has an average composition of $\text{En}_{31.2 \pm 7.9} \text{Wo}_{32.1 \pm 3.8} \text{Fs}_{36.7 \pm 10.2}$ (Table 7). In NWA 12335, high-Mg cores (both pigeonite and augite) have an average composition of $\text{En}_{31.9 \pm 10.8} \text{Wo}_{26.1 \pm 7.5} \text{Fs}_{42 \pm 13}$ while the high-Fe rims (pyroxferroite) have an average composition of $\text{En}_{5 \pm 1.5} \text{Wo}_{17.9 \pm 5.7} \text{Fs}_{77.2 \pm 6.1}$ (Table 8).

The pyroxenes in both NWA 10441 and 12335 show LREE-depleted REE profiles (Tables 9 and 10; Fig. 4). However, the patterns are different between the (pigeonite and augite) cores and the (Fs-pigeonite and pyroxferroite) rims. In NWA 10441, both the pigeonite and augite cores are enriched in LREE ($[\text{La}/\text{Lu}]_{\text{CI}} = 0.162$ and 0.14, respectively) relative to the Fs-pigeonite rims ($[\text{La}/\text{Lu}]_{\text{CI}} = 0.029$), which show an increased abundance in the HREE. A similar pattern is seen in NWA 12335, with $[\text{La}/\text{Lu}]_{\text{CI}}$ of 0.079 for pigeonite/augite cores compared to 0.006 for pyroxferroite rims. Pyroxene in NWA 12335 has a positive Eu anomaly ($\text{Eu}/\text{Eu}^* = >2$) compared to a slightly negative Eu anomaly in NWA 10441 pyroxene ($\text{Eu}/\text{Eu}^* = <1$).

Maskelynite

Maskelynite in both samples retains the original plagioclase subhedral to euhedral (up to 2–3 mm) morphology. More obvious in NWA 12335 but also noted in NWA 10441, maskelynite typically has the lath crystal shape of plagioclase. There is core to rim zoning of high-Ca (An) cores with high-K (Or) and -Na (Ab) rims. In both samples, but more extensively in NWA 12335, on the edges of the maskelynite grains, K–Si–glass has formed at the expense of the maskelynite. This has given the maskelynite an almost “cubic” appearance (Fig. 7). Maskelynite regions have a compositional range of $\text{An}_{44.2 \pm 7.8} \text{Ab}_{52.8 \pm 6.8} \text{Or}_{3.1 \pm 4}$ (in NWA 12335) and $\text{An}_{46.9 \pm 6.1} \text{Ab}_{49.5 \pm 5.4} \text{Or}_{3.5 \pm 2.5}$ (in NWA 10441). The large standard deviations, especially in the orthoclase component, reflect potassium zoning within the grains, which is more prominent in NWA 12335. In NWA

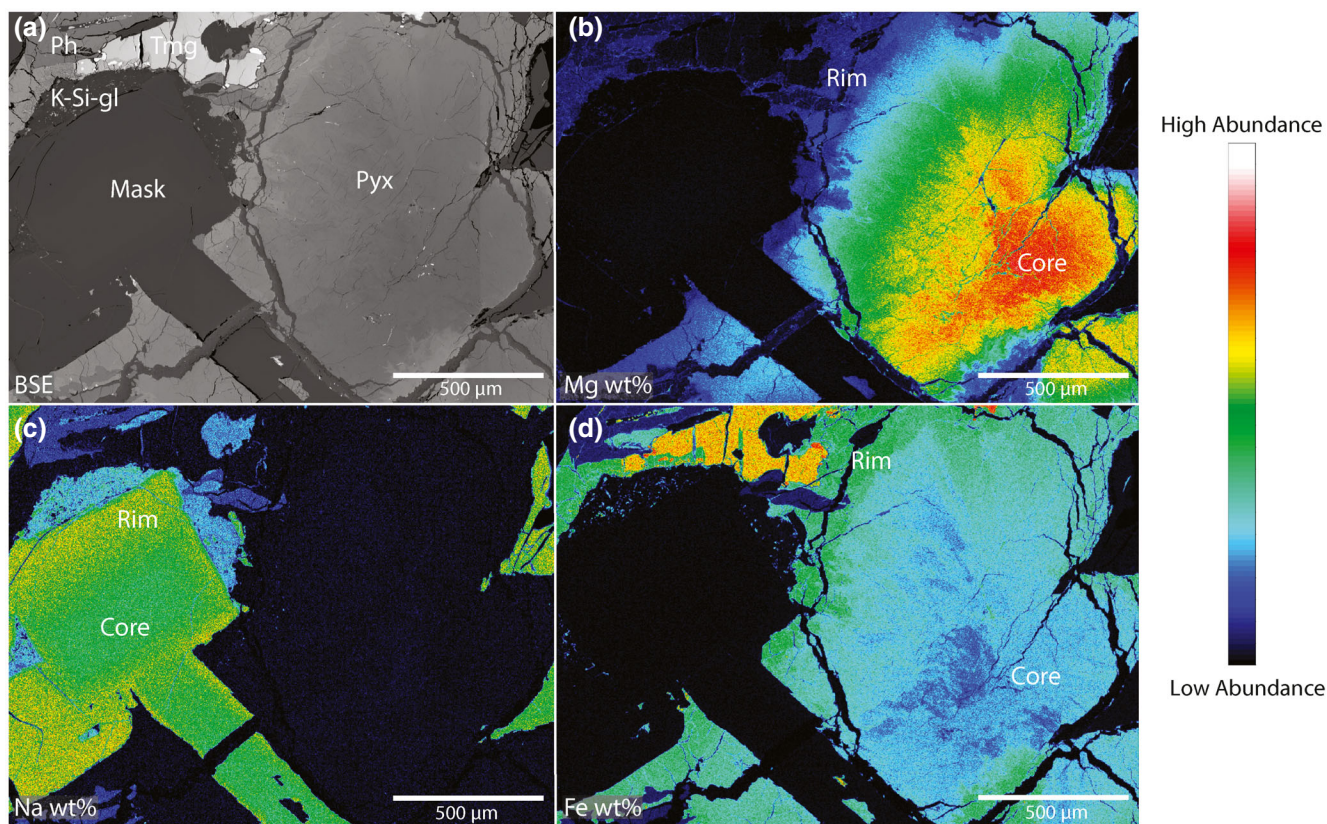


Fig. 7. EPMA quantitative element wt% maps of NWA 12335. a) BSE map displaying the mineralogy. b) Mg wt% map showing the trend in pyroxene from an Mg-rich core to an Mg-poor rim. c) Na wt% map showing compositional zoning in maskelynite. d) Fe wt% map showing the complex zoning within the pyroxene grain. There are no distinct boundaries between augite and pigeonite. Pyroxferroite forms as the rim of the pyroxene. Ph = phosphate; Tmg = titanomagnetite; K-Si-gl = K-Si-glass; Mask = maskelynite; Pyx = pyroxene. (Color figure can be viewed at wileyonlinelibrary.com.)

10441, maskelynite is enriched in the LREE with $[La/Lu]_{CI} = 4.72$ and also has a positive Eu anomaly ($Eu/Eu^* = 41.09$) (Fig. 6). In NWA 12335, Sm and the HREE from Tm-Lu are below LOD, although a positive Eu anomaly might be inferred (Fig. 6).

Phosphates

The phosphates are up to 1 mm long in NWA 10441 and up to 3 mm long in NWA 12335, with an abundance of 3% and 6%, respectively. The phosphate grains are anhedral, elongate crystals, generally found in the interstices between pyroxene and maskelynite. NWA 10441 and NWA 12335 contain both merrillite and chlorapatite with the latter representing $\sim 1/3$ of the phosphate in both meteorites. As is normal for phosphate minerals, REE abundances in both meteorites are extremely high ($>300_{CI}$). The REE profile of phosphates in NWA 10441 and NWA 12335 is relatively flat, both showing an enrichment in the LREE ($[La/Lu]_{CI} = 1.66$ and 1.68 , respectively). They also have a slightly negative Eu anomaly ($Eu/Eu^* = \sim 0.7$).

Accessory Phases

Accessory phases in the diabasic shergottites contribute $\sim 8\%$ of the mineralogy for both NWA 10441 and NWA 12335. Titanomagnetite grains can be up to 0.5 mm long, the majority of which ($>90\%$) also contain crosscutting exsolved ilmenite, which can be up to 20 μm thick. Chromite is near-absent, with very small $<10 \mu m$ grains present. Pyrrhotite is present with grain sizes $<300 \mu m$. Silica is observed in both NWA 10441 and NWA 12335, with grain sizes $\sim 300 \mu m$. Throughout NWA 12335, K-Si-glass is also present (Fig. 10). The glass has an irregular boundary with the surrounding pyroxene grains, and has entrained small elongate ($<200 \mu m$) pyroxene grains. This has been similarly observed in Los Angeles and is thought to be shock-derived (e.g., Xirouchakis et al., 2002). The REE profile of silica in NWA 10441 is relatively flat with $[La/Lu]_{CI}$ of 0.8. K-Si-glass in NWA 12335 has a similar flat REE profile with $[La/Lu]_{CI}$ 0.7 (Fig. 6). Significant positive Eu anomalies are present in NWA 10441 silica ($[Eu/Eu^*]_{CI}$ of 6.6) and NWA 12335 K-Si-

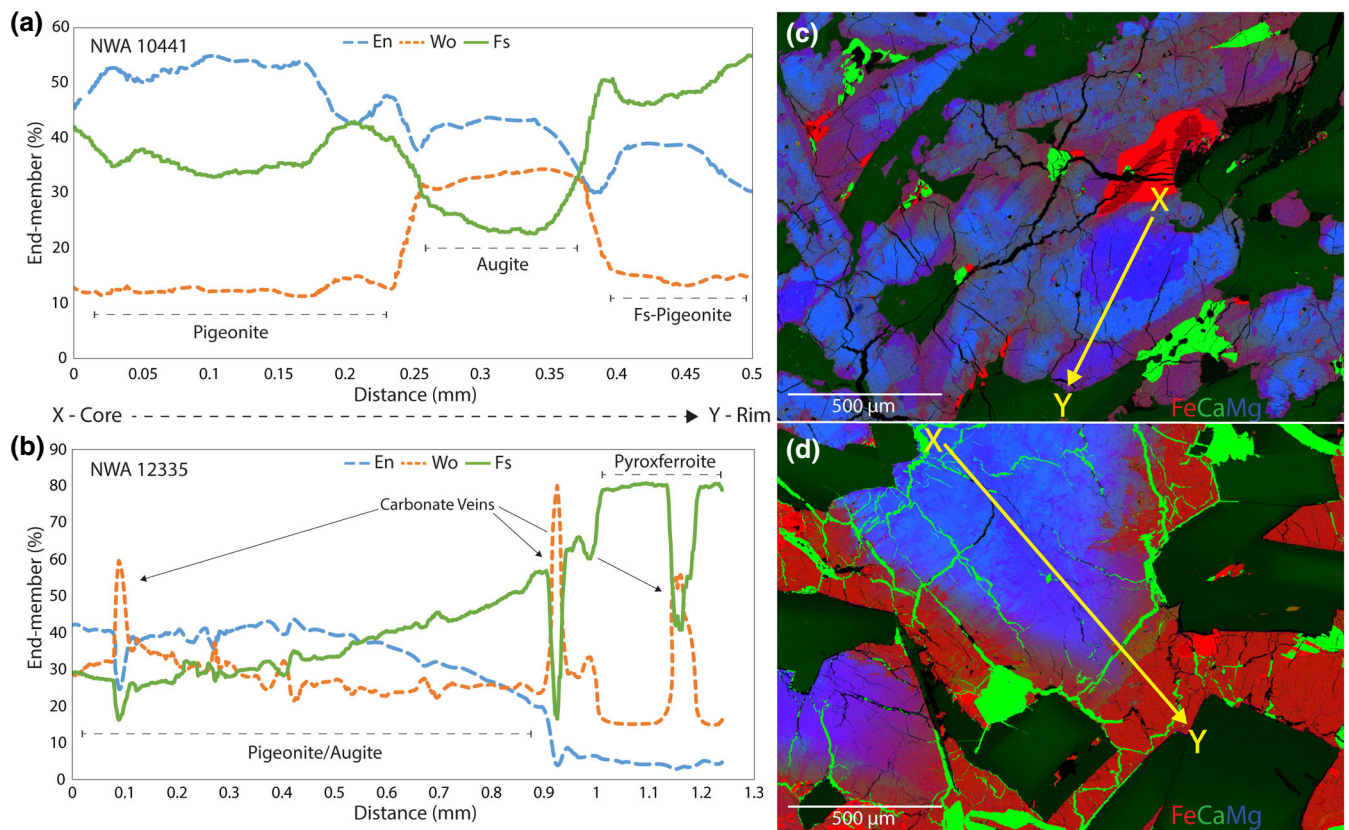


Fig. 8. Line profiles through combined EPMA quant maps in NWA 10441 and NWA 12335. a, b) Line profiles showing relative proportions of En, Wo, and Fs in the pyroxenes. c, d) Combined quant maps with X-Y line profiles indicated. Fe = red, Ca = green, and Mg = blue. (Color figure can be viewed at [wileyonlinelibrary.com](https://onlinelibrary.wiley.com/doi/10.1111/maps.13816).)

glass ($[\text{Eu}/\text{Eu}^*]_{\text{CI}}$ of 3.9). The large shock melt pocket (see below) in NWA 10441 also has a slight positive Eu anomaly with $[\text{Eu}/\text{Eu}^*]_{\text{CI}}$ of 1.5. Unlike the glass, the shock melt pocket has an overall LREE-depleted profile with $[\text{La}/\text{Lu}]_{\text{CI}}$ of 0.4.

Bulk REE

Understanding and defining the sources of the shergottites is important to exploring the magmatic history of Mars and, therefore, the evolution of the planet. The REE signatures of the shergottites are tied to their corresponding source reservoirs.

Because we had only thick and thin sections of the samples to work with, we determined chondrite-normalized REE profiles by combining in situ REE data of compatible minerals with modal mineralogy (e.g., Howarth et al., 2018). Two separate sets of bulk REE profiles were calculated based on the two methods used to determine modal mineralogy: thin section image point counting and 3-D image analysis using HRXCT results. Modal mineralogy derived from HRXCT was restricted to pyroxene, olivine, and maskelynite.

Phosphate grains could not be distinguished from pyroxene or olivine grains at the spatial resolution used for analyses primarily because the density of phosphate is very similar to the silicates (3.13 g cc^{-1} versus $\sim 3.3 \text{ g cc}^{-1}$). This is significant as phosphates are the main carrier of the REE budget in these rocks. Therefore, to account for this discrepancy as well as provide a calibration for our calculations, we compared our average modal mineralogy to published data sets of basaltic and poikilitic shergottites. If the olivine and pyroxene modal abundances were similar for our thin section/HRXCT abundances compared to published values, we assumed we could justifiably estimate the phosphate modal abundances of basaltic ($2.2 \pm 1.4\%$) and poikilitic ($1.1 \pm 0.5\%$) shergottites to use for our samples (Barrat, Jambon, et al., 2002; Harvey et al., 1996; Herd et al., 2017; Hui et al., 2011; Ikeda et al., 2006; Jambon et al., 2002; Lin et al., 2005; Llorca et al., 2013; McCoy et al., 1992; Mikouchi et al., 2001; Rahib et al., 2019; Rubin et al., 2000; Stöffler et al., 1986; Treiman et al., 1994; Udry et al., 2017; Usui et al., 2010; Wittke et al., 2006; Xirouchakis et al., 2002). This phosphate abundance was then subtracted from the HRXCT modal

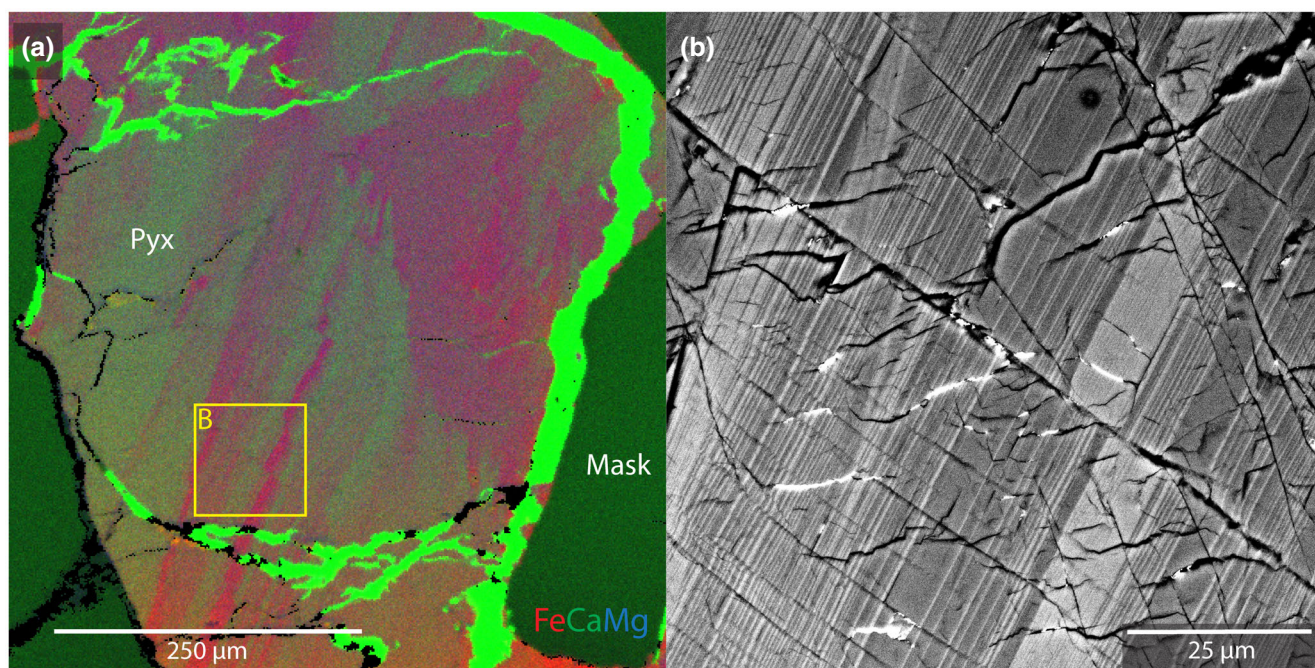


Fig. 9. Exsolution lamellae between augite and pigeonite in NWA 12335. a) Combined element map of a pyroxene grain showing lamellae and offsetting. Red = Fe, green = Ca, blue = Mg. Pyx = pyroxene; Mask = maskelynite; bright green = carbonate veining. b) BSE map (yellow box in [a] denotes location) of lamellae offset by a series of microfaults. (Color figure can be viewed at [wileyonlinelibrary.com](https://onlinelibrary.wiley.com/doi/10.1111/ramp.13816).)

Table 7. Representative major element compositions of the mineralogy in NWA 10441.

Oxide wt%	Pigeonite	Augite	Maskelynite	Merrillite	Apatite	Silica	Titanomagnetite	Ilmenite
SiO ₂	47.66	48.7	55.58	0.03	0.5	93.92	0.14	0.19
TiO ₂	0.46	0.43	0.04	–	–	0.26	27.18	45.7
Al ₂ O ₃	0.65	1	25.68	0	0.01	2.52	1.68	0.59
Cr ₂ O ₃	0.13	0.28	0	–	–	0.06	0.38	0.27
MgO	9.29	10.74	0.08	1.47	0.05	0.05	0.33	0.47
FeO	32.41	22.22	0.86	4.21	1.05	0.38	69	51.44
MnO	0.9	0.68	0.01	0.17	0.12	0.11	0.56	0.59
CaO	7.89	15.29	10.02	46.47	53.33	0.46	0.09	0.12
Na ₂ O	0.2	0.3	5.31	1.34	0.17	1.38	0.17	0.16
K ₂ O	0.04	0.04	0.48	–	–	0.53	0.03	0.03
P ₂ O ₅	–	–	–	46.88	41.86	–	–	–
F	–	–	–	0.07	2.73	–	–	–
Cl	–	–	–	–	1.66	–	–	–
Total	99.64	99.67	98.06	100.64	101.47	99.67	99.56	99.55
An			49.34					
Ab			47.73					
Or			2.93					
Wo	17.16	32.08						
En	27.76	31.24						
Fs	55.08	36.68						

abundance of pyroxene and olivine based on their relative proportions.

Comparing the results of HRXCT modal mineralogy against the numbers derived from thin

section is important for accuracy evaluation. Aside from phosphates, we can ignore the accessory phases as their REE contribution is negligible. Taking heterogeneity within samples into account, the relative HRXCT

Table 8. Representative major element compositions of the mineralogy in NWA 12335. Note, pyroxene core is an average of both augite and pigeonite.

NWA 12335									
Oxide wt %	Pyroxene core	Pyroxferroite rim	Maskelynite	Merrillite	Apatite	Chlorapatite	Silica	Titanomagnetite	Ilmenite
SiO ₂	48.27	45.07	55.17	0.22	0.91	0.98	92.72	0.3	0.47
TiO ₂	0.39	0.36	0.03	–	–	–	0.19	25.9	49.28
Al ₂ O ₃	1.06	0.65	25.92	0.07	0.06	0.06	2.8	1.76	0.38
Cr ₂ O ₃	0.09	0.05	0	–	–	–	0.06	0.07	0.06
MgO	10.66	1.55	0.08	0.61	0.03	0.03	0.04	0.17	0.24
FeO	26.66	42.84	0.61	5.69	1.22	1.12	0.45	70.48	48.23
MnO	0.76	1.04	0	0.15	0.14	0.08	0.08	0.67	0.69
CaO	11.35	7.76	9.99	45.14	51.61	51.16	0.47	0.12	0.18
Na ₂ O	0.32	0.21	5.61	1.34	0.21	0.33	2.03	0.18	0.18
K ₂ O	0.04	0.06	0.27	–	–	–	0.72	0.06	0.07
P ₂ O ₅	–	–	–	44.09	40.15	39.77	–	–	–
F	–	–	–	0.12	1.27	0.34	–	–	–
Cl	–	–	–	0.01	2.51	3.82	–	–	–
Total	99.6	99.59	97.68	97.43	98.12	97.68	99.58	99.71	99.76
An			48.83						
Ab			49.62						
Or			1.55						
Wo	26.07	17.87							
En	31.91	4.97							
Fs	42.02	77.16							

Table 9. Representative REE abundance (ppm) in minerals from NWA 10441, n equals the number of analyses averaged.

NWA 10441	Pigeonite core	Augite core	Fs-Pigeonite rim	Phosphate	Maskelynite	Shock melt	Silica
<i>n</i>	17	11	8	14	12	6	6
La	0.101	0.114	0.051	153.373	0.156	0.571	1.279
Ce	0.255	0.368	0.225	370.810	0.310	1.421	3.024
Pr	0.043	0.080	0.050	53.158	0.032	0.207	0.360
Nd	0.260	0.556	0.361	267.090	0.152	1.095	1.543
Sm	0.141	0.325	0.255	99.144	0.037	0.503	0.581
Eu	0.063	0.135	0.088	27.940	0.563	0.325	1.768
Gd	0.322	0.703	0.613	155.950	0.062	0.920	1.108
Tb	0.072	0.143	0.144	26.633	0.009	0.188	0.184
Dy	0.572	1.066	1.168	174.830	0.057	1.414	1.404
Ho	0.135	0.231	0.284	35.196	0.012	0.310	0.313
Er	0.421	0.655	0.912	95.383	0.033	0.932	0.987
Tm	0.063	0.091	0.148	12.214	0.005	0.134	0.154
Yb	0.441	0.577	1.119	72.577	0.028	0.905	1.190
Lu	0.066	0.086	0.188	9.827	0.004	0.138	0.162

abundances of maskelynite, olivine, and pyroxene in all the meteorites are similar to thin section abundances (within ~15%). The most significant discrepancy is for olivine abundance in NWA 10818, with XCT of ~65 vol % and thin section of ~44 vol%. Due to the poikilitic texture and size of the sample, the thin section slice is less likely to be a true representation of the modal

amount. Furthermore, due to the low overall abundance of REE in the major mineralogy compared to phosphate, these differences will not have a significant impact on the bulk REE profiles.

Using thin section-derived modal mineralogy bulk REE, NWA 10441 and NWA 12335 display an enriched REE profile, with a flat REE pattern ([La/Lu]_{CI} of 1.49

Table 10. Representative REE abundance (ppm) in minerals from NWA 12335, *n* equals the number of analyses averaged.

NWA 12335	Pyroxene core	Pyroxferroite rim	Phosphate	Maskelynite	K–Si–glass
<i>n</i>	31	13	20	14	9
La	0.077	0.038	128.686	0.098	1.227
Ce	0.308	0.146	310.170	0.170	2.867
Pr	0.067	0.030	44.356	0.016	0.371
Nd	0.481	0.205	221.921	0.067	1.653
Sm	0.338	0.178	84.368	b.d.	0.604
Eu	0.395	0.222	25.072	0.522	0.957
Gd	0.715	0.516	133.764	0.001	0.944
Tb	0.149	0.152	23.139	b.d.	0.201
Dy	1.134	1.554	153.352	b.d.	1.628
Ho	0.248	0.448	30.867	b.d.	0.350
Er	0.734	1.873	83.886	b.d.	1.086
Tm	0.103	0.382	10.640	b.d.	0.175
Yb	0.697	3.510	62.060	b.d.	1.223
Lu	0.105	0.646	8.146	b.d.	0.183

b.d. = below detection limit.

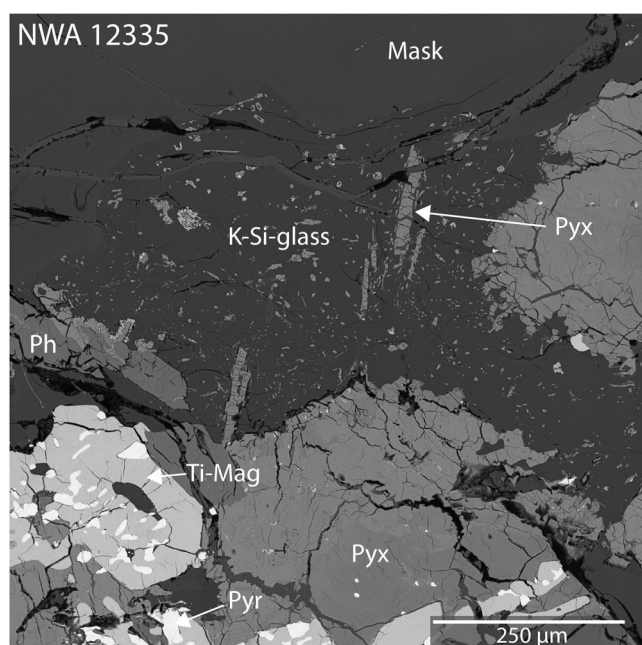


Fig. 10. BSE map of NWA 12335 showing the textural relationships of K–Si–glass. Note the pyroxene grains inside the glass and the irregular boundary between the glass and pyroxene grains. Ph = phosphate; Mask = maskelynite; Pyx = pyroxene; Ti-Mag = titanomagnetite; Pyr = pyrrhotite.

and 1.38, respectively). NWA 10818 and NWA 11043 display an intermediate profile, with a depletion in LREE relative to HREE ($[La/Lu]_{CI}$ of 0.49 for both). NWA 12335 has the highest overall bulk abundance of REE, while NWA 11043 is least abundant, with a slight enrichment in La.

Using the HRXCT-derived modal mineralogy, we observe similar overall REE profiles for the meteorites,

Table 11. Calculated bulk (using HRXCT) REE abundances (ppm) in NWA 10441, NWA 10818, NWA 11043, and NWA 12335.

	NWA 10441	NWA 10818	NWA 11043	NWA 12335
Bulk				
La	3.434	0.380	0.600	2.869
Ce	8.320	0.975	1.192	6.944
Pr	1.199	0.151	0.210	1.000
Nd	6.082	0.925	1.237	5.063
Sm	2.305	0.569	0.722	1.990
Eu	0.829	0.265	0.365	0.947
Gd	3.728	1.108	1.381	3.264
Tb	0.652	0.206	0.257	0.585
Dy	4.366	1.432	1.757	4.020
Ho	0.896	0.292	0.356	0.839
Er	2.471	0.806	0.980	2.409
Tm	0.325	0.106	0.128	0.333
Yb	1.995	0.675	0.792	2.187
Lu	0.279	0.097	0.112	0.322

despite a change in their relative abundance of REE (Table 11; Fig. 11). Although the overall REE abundances of NWA 10441 and 12335 have decreased compared to thin section-derived bulk REE, their profiles are more in line with other enriched shergottites with $[La/Lu]_{CI}$ of 1.31 and 0.95, respectively (e.g., Cao et al., 2018; He et al., 2015). The REE profile of NWA 10441 is closer to the “measured” bulk REE profile of suggested pair NWA 8657 (Howarth et al., 2018). Similarly, HRXCT-derived bulk REE of NWA 10818 and NWA 11043 are more typical of intermediate shergottites, with $[La/Lu]_{CI}$ of 0.42 and 0.57, respectively (e.g., Filiberto et al., 2012; Riches et al., 2011).

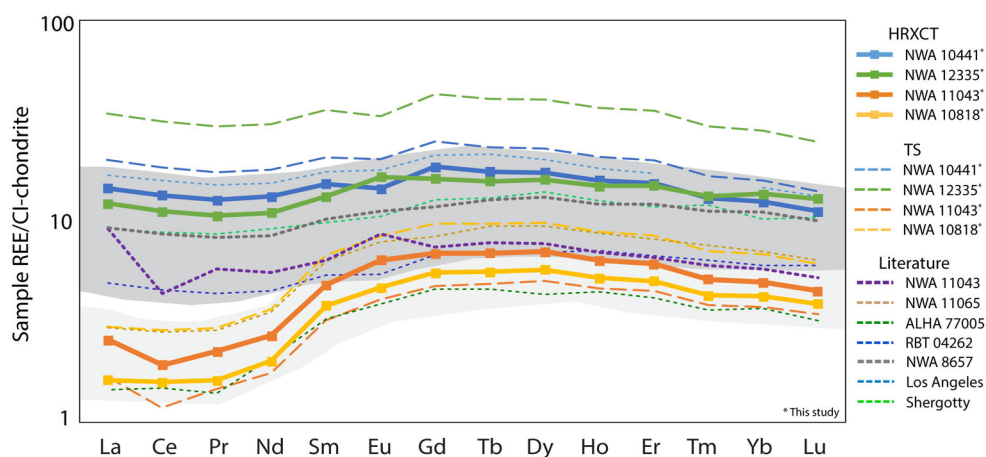


Fig. 11. Chondrite-normalized HRXCT and TS (thin section) calculated bulk REE profiles of the new shergottites compared against other enriched and intermediate, basaltic and poikilitic, shergottites (Anand et al., 2008; Howarth et al., 2018; Jambon et al., 2002; Lodders, 1998; Rahib et al., 2019). Dark gray = enriched, light gray = intermediate. (Color figure can be viewed at wileyonlinelibrary.com.)

DISCUSSION

This study reinforces and expands on the preliminary classifications of these meteorites (MetBull 104–107). Below we discuss the crystallization history, shock evidence, and weathering, and how these processes have impacted the geochemical composition of these rocks.

Crystallization History: Extrusive Versus Intrusive

The poikilitic shergottites, NWA 10818 and NWA 11043, appear to have experienced similar crystallization histories to other poikilitic shergottites (e.g., Howarth et al., 2014; Rahib et al., 2019; Riches et al., 2011; Walton et al., 2012). The high-Fo olivines together with high-Mg#, high-Cr# chromites are consistent with these minerals being first to crystallize in the melt, followed by low-Ca pyroxene (pigeonite). The pyroxene enclosed the smaller olivine and chromite chadacrysts, forming large pyroxene oikocrysts. The presence of elemental zoning suggests high-Ca pyroxene (augite) crystallized as overgrowths on the pigeonite oikocrysts. As interstitial melt accumulated, the cumulate oikocrysts and olivine (not enclosed by pyroxene) were entrained in the rising magma. From these interstitial melts, nonpoikilitic pyroxene (pigeonite and augite) and plagioclase co-crystallized. The accessory phases also started to crystallize from the evolved melt. The poikilitic regions are more primitive with higher Mg#, Fo%, and Cr# (pyroxene, olivine, and chromite, respectively) compared to the nonpoikilitic regions. Based on the Ti/Al ratios of the poikilitic pyroxene (pigeonite and augite) in NWA 10818 and NWA 11043, the poikilitic regions crystallized first, most likely in the lower Martian crust close to the upper mantle boundary

(Filiberto et al., 2010; Rahib et al., 2019). The nonpoikilitic regions crystallized as melt accumulated during magma ascent up through the crust with final emplacement in a hypabyssal system near the surface (e.g., Lin et al., 2013).

The diabasic shergottites (NWA 10441 and NWA 12335) each had a slightly different petrogenesis, but their overall genesis was similar to other basaltic shergottites (e.g., Barrat, Jambon, et al., 2002; McCoy et al., 1992; McSween et al., 1996). Like most other basaltic shergottites, olivine is not present. Based on the low Mg#s of the pyroxene, NWA 10441 and NWA 12335 must have crystallized from an evolved melt. This melt has been suggested to have already experienced olivine fractionation (e.g., Treiman & Filiberto, 2015). In NWA 10441, the distinct Mg-rich augite and pigeonite cores were first to crystallize in the melt. These grains were then entrained in magma as it ascended toward the surface. As the magma rose, more Fe-rich augite and pigeonite started to form mantles around the cores. Fs-pigeonite (in the forbidden zone) rims were last to crystallize, forming as a result of extrusion of the magma onto the Martian surface. Fe-rich pyroxene compositions are metastable at pressures <10 kbar (Lindsley & Burnham, 1970), so crystallization without subsequent breakdown requires extremely rapid cooling, conducive to an eruption or extrusion of lava onto the surface. This also applies to pigeonite. NWA 10441 shows evidence of a two-stage crystallization history, with Mg-rich pyroxene cores crystallizing at depth, developing into more Fe-rich pyroxene as the magma ascended. A multistage crystallization does not necessarily require an open magmatic system. Similar shergottites to NWA 10441, such as NWA 5298 and Zagami, may have formed in a closed system, with

sudden magma movement (i.e., eruption) initiating the final stage of crystallization (Hui et al., 2011; McCoy et al., 1992). This could also be the case for NWA 10441; however, further petrological investigation is required to fully constrain the magmatic evolution.

NWA 12335 has a slightly different crystallization history. The zoning in the pyroxene is much more complex and is similar to that of Los Angeles and Queen Alexander Range (QUE) 94201 (e.g., Kring et al., 2003; McSween et al., 1996; Mikouchi et al., 1998; Warren et al., 2004). Mg-rich pyroxene cores initially crystallized. As the magma ascended to the surface, there is a trend toward more Fe-rich pyroxene crystallization. Unlike NWA 10441, there are no sharp boundaries between augite and pigeonite zoning. The interstitial growth of compositionally different pyroxenes implies that Ca-rich (augite) and Ca-poor (pigeonite) pyroxene co-crystallized, forming compositionally heterogeneous pyroxene grains. Ca-rich pyroxene only stopped crystallizing at the onset of plagioclase crystallization, as Ca would be preferentially incorporated into plagioclase over pyroxene. Prior to plagioclase crystallization, the melt was becoming enriched in Fe. Similar to NWA 10441, Fs-pyroxene compositions crystallized toward the rims of the pyroxene grains. However, in NWA 12335, due to very high-Fe enrichment, pyroxferroite was the final phase to crystallize on the rims of the pyroxene grains. Pyroxferroite (and plagioclase) must have crystallized rapidly as the magma cooled on eruption onto the Martian surface. As previously stated, these high-Fe rich pyroxene phases (and pigeonite itself) are metastable at low temperature and pressure. Pyroxferroite rims have been reported on a number of Martian and lunar meteorites, suggesting that these conditions are prevalent on these bodies (e.g., Liu et al., 2009; McSween et al., 1996). The crystallization sequence of NWA 12335 suggests the melt crystallized in a closed system, similar to QUE 94201 (e.g., Kring et al., 2003). This is interpreted to represent continuous crystallization instead of multistage crystallization (e.g., McSween et al., 1996).

Rare Earth Element Determination

Although thin section-derived bulk REE profiles indicate which REE/incompatible trace element group these new shergottites belong to, the overall REE abundance is inaccurate. The modal mineralogy seems to overestimate phosphate abundance (and hence REE abundance) for NWA 10441, NWA 10818, and NWA 12335, and underestimates the amount of phosphate in NWA 11043. This is most likely due to the inherent heterogeneity of phosphate distribution at these scales within these samples. HRXCT-derived bulk REE profiles using inferred phosphate abundances are more

representative of the whole rock. Hence, HRXCT is the preferred technique for bulk compositions, as the distribution of mineralogy can be more comprehensively determined. Thin section modal abundances, especially for small samples that contain large grains (poikilitic shergottites), tend to not be representative of the original rock.

Using the HRXCT-modal abundance, the calculated REE profile of NWA 11043 is different to previously reported results for NWA 11043 (Rahib et al., 2019). We do not observe the same relative enrichment in LREE, though we observe very similar HREE abundances and the same La enrichment and Ce depletion pattern. Rahib et al. (2019) reported an $[La/Lu]_{CI}$ of 1.76 for NWA 11043, compared to an $[La/Lu]_{CI}$ of 0.57 using the HRXCT-calculated REE profile. To understand the discrepancy between the different results, we modeled the bulk REE profile with varying abundances of minerals using our in situ LA-ICP-MS REE results.

Since phosphate is the primary carrier of REE, small changes in the modal abundance will have a larger effect on the bulk. In addition to the abundance of phosphate, we note that 2 of the 11 phosphate analyses show a different pattern in the LREE (Fig. 12). If these two phosphate compositions are the only analyses used in the calculations, we can create an inferred REE profile using ~20% pyroxene, ~50% olivine, ~30% maskelynite, and ~1.3% phosphate (Fig. 12), which is closer to the bulk REE reported by Rahib et al. (2019). This approach raises the question of how representative the individual phosphate compositions are compared to the whole rock. Either REE were not evenly distributed in the phosphates during crystallization or phosphate abundances throughout the rock are heterogeneous and therefore even measured bulk REE of chips (generally <1.5 g) may not be representative of the whole rock. Alternatively, secondary processes may be responsible, such as shock processes and geochemical weathering, for the heterogeneous phosphate REE abundances in NWA 11043.

Shock Deformation Features

Shock deformation in meteorites is an extremely important process that can cause immediate and wide-ranging deformational changes to the mineralogy and texture of the meteorites. Understanding and characterizing the effects of shock is important to reconstructing the history of these meteorites, and also to identifying the difference between primary and secondary features. With only a few exceptions (NWA 8159, e.g., Herd et al., 2017), most shergottites have experienced significant levels of shock (e.g., El Goresy et al., 2013).

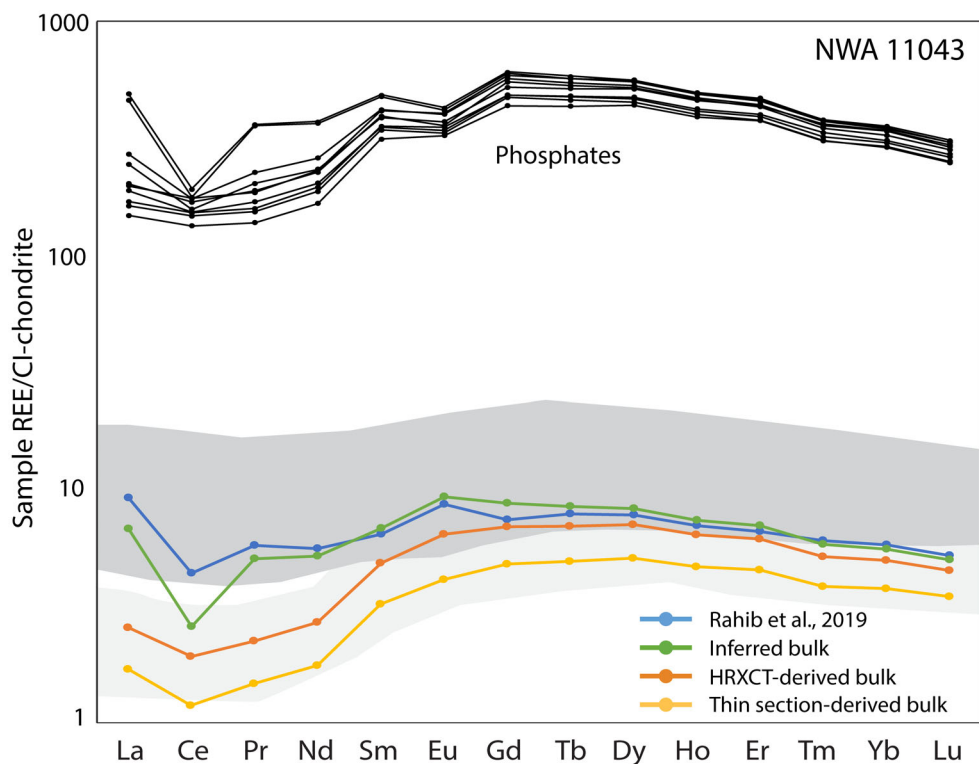


Fig. 12. LREE enrichment in NWA 11043 compared to bulk REE patterns using different modal abundances. All of the in situ (this study) phosphate analyses are displayed. Note the two analyses with a relative LREE enrichment. The measured bulk spectra (Rahib et al., 2019) are compared against an inferred bulk (only including the two LREE-enriched phosphate analyses) and the HRXCT- and thin section-derived bulk REE profiles (not including the two LREE-enriched phosphates). Note the shift from enriched (dark gray) to intermediate (light gray) depends on which phosphates are used in the calculated bulk REE profiles. (Color figure can be viewed at wileyonlinelibrary.com.)

Shergottite shock features likely relate to the meteorite's liberation from Mars (e.g., Fritz et al., 2005). Ejection from the Martian surface requires a powerful impact to induce the 5 km s^{-1} escape velocity (Artemieva & Ivanov, 2004). An impact crater diameter of 3 km has been purported as the minimum size of an impact event for successful ejection of rock fragments and their subsequent encounter with Earth (Head et al., 2002). Evidence of these impacts are often recorded as shock deformation in the Martian rock fragments recovered on Earth.

The most obvious shock feature in the studied shergottites is the shock metamorphism of plagioclase to diaplectic glass, maskelynite. According to Stöffler et al. (2018), diaplectic glass forms in plagioclase from 24/34 GPa (increasing from anorthite to albite) to ~45 GPa. Maskelynite in NWA 10441 (~An₄₇) and NWA 12335 (~An₄₄) has an average andesine composition, while in NWA 10818 (~An₅₀) and NWA 11043 (~An₅₇), maskelynite has an average labradorite composition. If taking account of the maskelynite zoning in NWA 10441 and NWA 12335, a similar

minimum shock pressure of ~30 GPa could be ascribed to all.

Pervasive fracturing can be seen throughout the samples, with varying degrees of severity. The basaltic shergottites (NWA 10441 and NWA 12335) have irregular and subplanar fracturing (concentrated in the pyroxene grains), with increased fracturing on the rims of the pyroxene grains (Fig. 13). The poikilitic shergottites (NWA 10818 and NWA 11043) exhibit a higher degree of fracturing. Extensive planar fractures are observed in both pyroxene and olivine. In pyroxene, not all the fracturing is the result of shock. Some of the observed fracturing will be related to cleavage, though as planes of weakness, these “cleavage fractures” would be more pronounced. According to Stöffler et al. (2018), planar fractures in olivine and pyroxene are caused by a minimum shock pressure of 5–10 GPa.

In all of the studied shergottites, mechanical twinning in pyroxene is observed. The most pronounced twins are found in NWA 11043, where a pyroxene oikocryst has twinning in the (100) plane (Fig. 14). In the other pyroxene oikocryst in NWA 11043, no

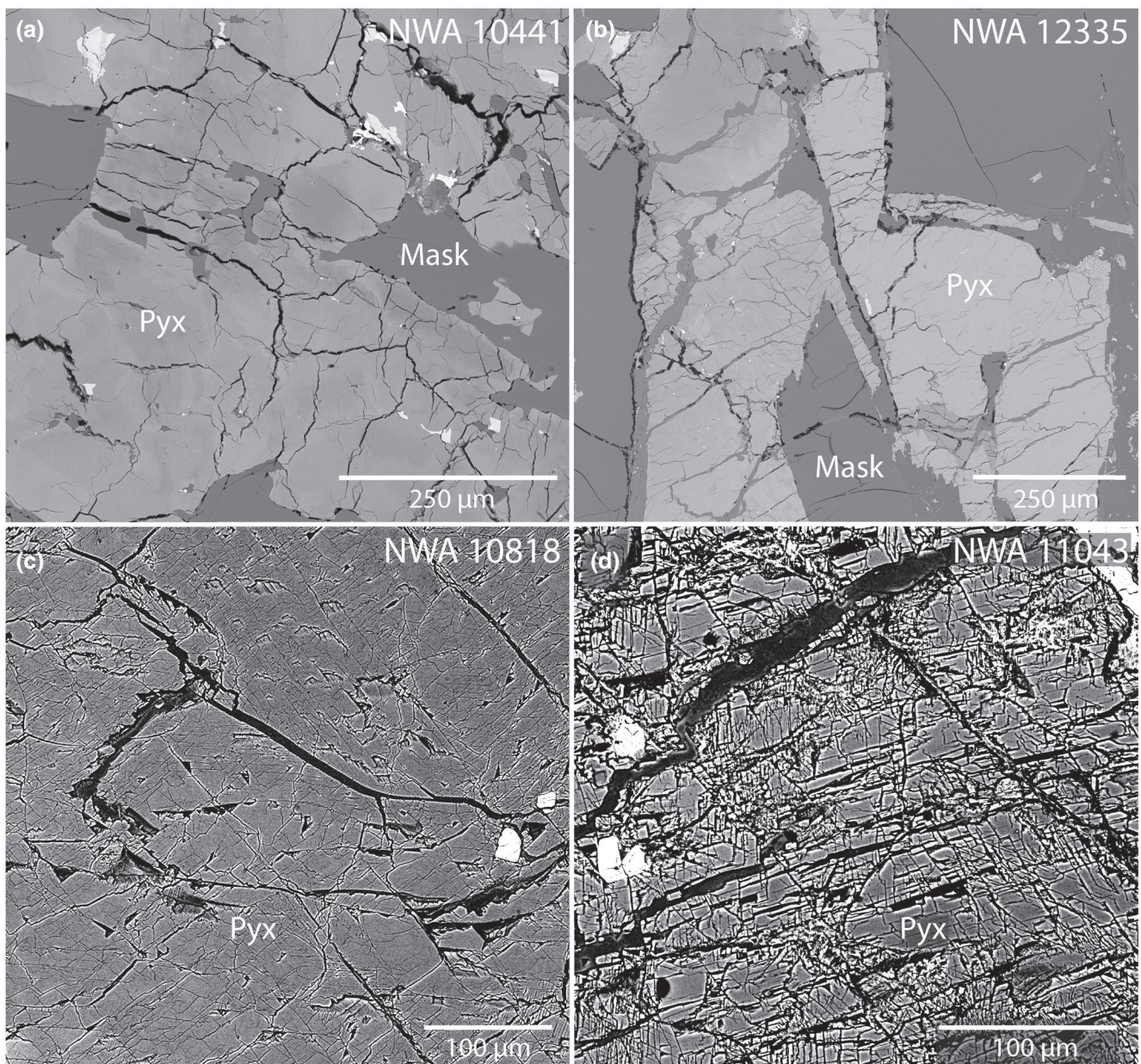


Fig. 13. BSE maps showing distribution and intensity of fracturing. a, b) The diabasic shergottites with irregular to subplanar fracturing in pyroxene and little fracturing in maskelynite. c, d) Pyroxene oikocryst grains in the poikilitic shergottites displaying irregular and planar fracturing. Images were stretched to highlight extent of fracturing. NWA 11043 has a higher degree of fracturing compared to NWA 10818. Pyx = pyroxene; Mask = maskelynite.

twinning is observed. These oikocrysts have different crystallographic orientations, and consequently, the grains may have reacted differently to the shock wave as it propagated through the rock, causing a heterogeneous distribution of mechanical twins. The twins in NWA 11043 are much wider than the twins in the other shergottites (up to 20 μm compared to <5 μm , respectively) and they are also much longer (up to 150 μm compared to <20 μm , respectively). However,

mechanical twinning in pyroxene can form at pressures from 5 to 70 GPa, so they cannot be used as a reliable pressure indicator (Stöffler et al., 2018).

NWA 10441 contains shock melt pockets throughout the sample, the largest being nearly 2 mm wide (Fig. 15). On the rim of the large shock melt pocket, there is an obvious zone where the pyroxene grains recrystallized into smaller grains within their original host grains. EBSD orientation analysis

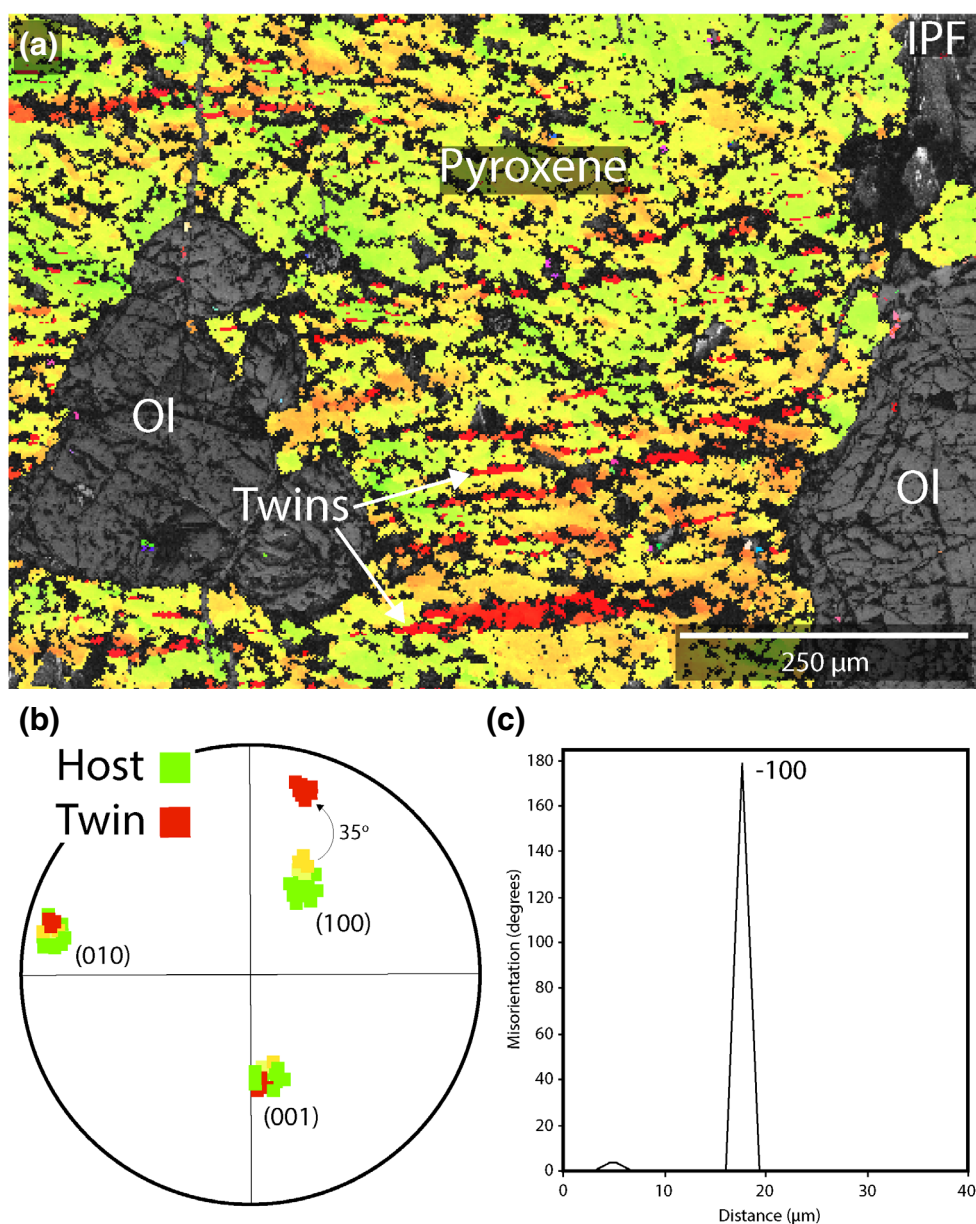


Fig. 14. Pyroxene shock twins in NWA 11043. a) EBSD orientation map, with an inverse pole figure (IPF) color scheme, of a pyroxene oikocryst displaying (100) shock twins (in red). The black features are fractures that did not index during EBSD analysis. Ol = olivine. b) Pole figure of the host pyroxene and shock twin orientations. The stereonet is an equal area, lower hemisphere projection plotted in sample reference frame. c) Misorientation profile of a pyroxene (100) shock twin in a pyroxene host grain. (Color figure can be viewed at wileyonlinelibrary.com.)

highlighted the finer recrystallized grains in the relict larger pyroxene grains. The zone of recrystallization extends to $\sim 200 \mu\text{m}$ from the shock melt pocket. The boundary between this zone and the shock melt pocket is sharp, with the pyroxene and maskelynite grains inside the shock melt pocket becoming interwoven (Fig. 15). Shock melt pockets have also been reported in the suggested pair to NWA 10441, NWA 8657 (Howarth et al., 2018). Higher pressures and temperatures within

the shock melt pocket have instigated partial melting of the pyroxene and maskelynite. Heterogeneous elemental distribution within the melt pocket suggests only partial integration of pyroxene and maskelynite grains into a melt glass. Due to the mafic polymineralic nature of NWA 10441, there is a large range in shock impedance (ability of the mineral to propagate the shockwave) of the major mineralogy (plagioclase and pyroxene). During shock wave propagation, this impedance range

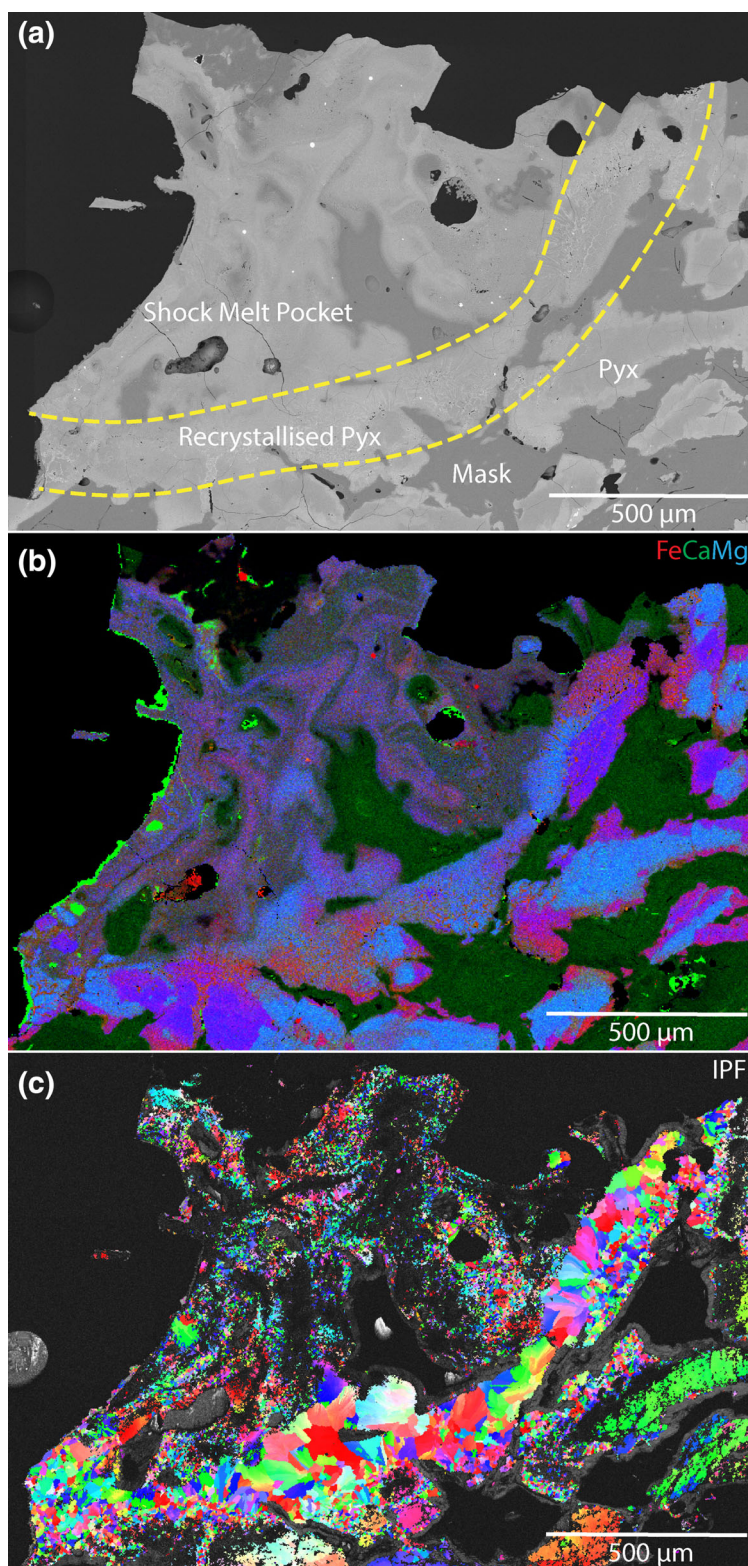


Fig. 15. Shock melt pocket in NWA 10441. a) BSE map of the shock melt pocket. Pyx = pyroxene; Mask = maskelynite. Yellow dashed lines indicate rim of recrystallized pyroxene. Black “blobs” are gas vesicles. b) Combined elemental distribution map, Fe = red, Ca = green, and Mg = blue. c) EBSD-derived IPF (inverse pole figure) colored map showing the recrystallized zone around the shock melt pocket. The colors represent different crystallographic orientations of the pyroxene grains which also indicates grain boundaries. (Color figure can be viewed at wileyonlinelibrary.com.)

encourages localized melting where peak shock pressures can be much higher than the equilibrium shock pressure of the whole meteorite (e.g., Sharp & DeCarli, 2006). These pressures, likely exceeding ~ 70 GPa (Stöffler et al., 2018), caused high shock-induced temperatures, which triggered partial melting of the rock. The minimum temperature for melting nonporous basalt is 1600°C (Stöffler, 1984). The temperatures and pressure, therefore, represent the minimum conditions required to induce shock melting. Similar results were reported for Los Angeles where shock melt pockets were estimated to have formed at $60\text{--}80$ GPa and at $1600\text{--}2000^\circ\text{C}$ (Walton & Spray, 2003). Due to these high temperatures, neocrystallization of the surrounding pyroxenes through thermal metamorphism occurred, forming a rim around the shock melt pocket. Similar localized shock effects are not observed in all the basaltic shergottites. This may be because (1) shock pressures will vary between the rocks and (2) heterogeneity in the rocks and small sample sizes could be hiding these features. Based on the evidence observed, NWA 10441 experienced higher shock pressures than the other basaltic shergottite NWA 12335.

The shock pressure estimates for these shergottites are similar to other basaltic and poikilitic shergottites (e.g., Hui et al., 2011; Walton et al., 2012). All the meteorites experienced at least ~ 30 GPa, with an upper limit of ~ 45 GPa for NWA 10818 and NWA 11043, and <45 GPa for NWA 10441 and NWA 12335. NWA 10441 experienced the highest peak shock pressure of ~ 70 GPa, which caused localized melting. Based on the proposed stages of shock metamorphism by Stöffler et al. (2018), these shergottites are all in the S4 (mafic) shock stage, potentially pushing into S5. More investigation is required to further constrain shock pressures.

Geochemical Weathering in NWA 11043

Once meteorites land on Earth, terrestrial weathering will start to cause alteration within the rocks, the type and extent of which will differ depending on landing site. NWA 10441, NWA 10818, NWA 11043, and NWA 12335 were found in “Northwest Africa,” most likely in a desert environment. Therefore, they have all experienced (to different degrees) hot desert climate weathering. Weathering has the potential to create localized REE compositional effects within the rock (Croaz et al., 2003; Croaz & Wadhwa, 2001).

The introduction of a terrestrial REE component can lead to an LREE enrichment profile (Croaz et al., 2003). The distribution of the terrestrial REE component can be very heterogeneous, as it will be localized to areas that are proximal to fractures and veins, which would

have facilitated the REE redistribution. In situ analysis of minerals allows for a deeper understanding of the effects of this weathering process. The susceptibility of the REE abundance in minerals to be altered via this process is dependent on the mineral in question. Low REE abundance carriers are more likely to be affected. Olivine and pyroxene (overall REE abundance of $<1\times$ CI and $\sim 1\times$ CI, respectively) both display a relative enrichment in the LREE. Maskelynite is not generally affected, as the similar REE profile of NWA 11043 compared to the other new shergottites demonstrates. Phosphates, as the main carrier of REE, should not be affected by a small enrichment in LREE, as their REE abundances are $>100\times$ CI. However, in NWA 11043, we observe a variation in phosphate REE profiles, with 2 of 11 analyzed grains displaying an enrichment in LREE. This suggests that terrestrial input was significant enough to alter the REE profile of the phosphates, but heterogeneously. Interestingly, we do not observe the same LREE enrichment in the other new shergottites. Although displaying similar terrestrial weathering products, the REE profiles of the minerals do not show a terrestrial signature. This implies that NWA 11043 is more weathered than the other studied shergottites, which suggests it has had a longer terrestrial exposure time. However, longer exposure does not necessarily equate to increased level of alteration. Initial weathering is the most significant as the porosity of the meteorite will decrease over time due to alteration, which in turn, slows down the alteration process as there is less pore space (i.e., cracks) for alteration products to infill (Bland et al., 1996). Therefore, to explain the weathering differences we have to turn to shock processes, where differences might lead to variable alteration of rocks over the same amount of time.

All the meteorites display cracks and veins, but to different levels. NWA 11043 is the most heavily fractured, based on BSE mapping (Fig. 13)—so much so that the traditionally mafic crystalline rock with little to no porosity had been transformed to a rock with a high degree of “shock-induced porosity” (e.g., Rae et al., 2019). This substantial increase in porosity relative to the other meteorites would have encouraged more extensive alteration. This could explain why NWA 11043 has mineral LREE enrichment signatures and the other meteorites do not. At which exact point a weathered meteorite, for example, NWA 10818, develops a terrestrial REE signature similar to NWA 11043 is not obvious. Further work would be required to constrain the requisite conditions, which is beyond the scope of this paper.

Thus, by not “measuring” the bulk REE abundance of NWA 11043, and, instead, “calculating” the bulk REE abundance from in situ analysis, we can avoid

terrestrially altered minerals, and just attempt to include the most “Martian” REE abundances. We also avoid all the veins in the bulk calculation as these will be the main carriers of the terrestrial REE, and their inclusion is unavoidable during bulk analyses. Therefore, we propose that in highly weathered meteorites, combining the 3-D major modal mineralogy derived from HRXCT (or other high-resolution techniques) and an average phosphate abundance derived from most of the poikilitic shergottites with *in situ* REE analyses of specific target grains yields a more accurate bulk REE profile than measured bulk powdered analyses as weathering products can be avoided.

This being the case, we conclude that NWA 11043 has an intermediate REE profile and is not enriched as suggested by Rahib et al. (2019). The intermediate profile still bears a terrestrial weathering signature, with an enrichment in La and depletion in Ce, but overall fits in the intermediate field.

Is NWA 10441 Paired with NWA 8657?

NWA 10441 is suggested to be a pair of NWA 8657 (Bouvier, Gattacceca, Agee, et al., 2017; Bouvier, Gattacceca, Grossman, et al., 2017). Both meteorites were recovered in “Northwest Africa” in 2015 and 2014, respectively. A meteorite pair by definition is a part of the original meteorite that either fragmented during descent through Earth’s atmosphere or was eroded and transported via terrestrial processes away from the host meteorite (e.g., Benoit et al., 2000). Both of these meteorites were initially reported to comprise numerous stones. The locations of these stones in relation to each other are not reported; therefore, it is unknown if they were all found in the same place, or strewn across an area. If the latter, the original meteorite must have had multiple stages of fragmentation during its disintegration descending through the atmosphere (e.g., Babadzhanyan, 2002). Once the meteorites have landed, terrestrial weathering can occur. As previously stated, NWA 10441 contains very little evidence of terrestrial alteration. NWA 8657 is reported to contain pervasive carbonate weathering throughout the meteorite with positive Ba anomalies usually associated with hot desert weathering (Howarth et al., 2018). The meteorites could also have landed in areas with different weathering rates. Therefore, weathering differences may not be indicative of pairing or lack thereof.

Geologically speaking, both meteorites exhibit typical basaltic shergottite textures and compositions (Howarth et al., 2018). NWA 8657 and NW 10441 contain euhedral pyroxene (70 and 66.9%, respectively) and maskelynite (25 and 29%, respectively) grains that are both geochemically zoned. The pyroxenes have pigeonite or augite cores,

surrounded by ferrosilite-rich rims, with overlapping compositions between the meteorites. The maskelynite has high-An cores with high-Ab/Or rims. Accessory phases include phosphates, primarily merrillite, and oxides (pyrrhotite, ilmenite, titanomagnetite). Shock melt pockets and the presence of vesicles are observed throughout both meteorites (Howarth et al., 2018). Although very similar, other basaltic shergottites display similar characteristics making it inconclusive to ascribe pairing based on mineralogy and petrological evidence alone (e.g., Udry et al. [2020] and references therein).

The REE geochemistry of shergottites can also be used to test pairing. If they are paired, then their REE profile should be comparable. The HRXCT-derived REE profile of NWA 10441 is slightly more enriched in LREE, with an $[La/Lu]_{CI}$ of 1.31, compared to NWA 8657, which has a relatively flat REE profile with an $[La/Lu]_{CI}$ of 0.92. NWA 10441 also has a slight negative $[Eu/Eu^*]_{CI}$ anomaly of 0.86 compared to the flat 1.03 for NWA 8657. Even with minor differences, both NWA 10441 and NWA 8657 are enriched shergottites displaying similar REE distributions. As previously discussed, heterogeneity with the meteorites themselves, especially in relation to phosphates, creates a situation where minor differences are most likely not significant. For a conclusive match, the geochronological and ejection ages (cosmic ray exposure plus terrestrial age) of the meteorites would need to be investigated. As pairs, they would have the same or very similar corresponding ages. Without these ages, and given the previously stated evidence, NWA 8657 and NWA 10441 are likely meteorite pairs that landed in slightly different locations, producing variable weathering patterns.

CONCLUSIONS

In this study, we conducted a number of geochemical and mineralogical analyses to classify four new shergottites. We confirm that NWA 10818 and NWA 11043 are intermediate poikilitic shergottites. In contrast to Rahib et al. (2019), we find that NWA 11043 has an intermediate REE pattern. This is likely because it experienced significant terrestrial weathering, encouraged by extensive shock-induced fracturing, which caused enrichment in LREE, affecting its classification based on bulk analysis. By conducting *in situ* analyses of NWA 11043, we concluded that by avoiding terrestrially altered analyses, we could discern the altered versus unaltered pattern visible in the REE abundances. The crystallization history of NWA 10818 and NWA 11043 is similar to other poikilitic shergottites. The poikilitic areas crystallized first at depth, then the nonpoikilitic areas started to crystallize as the magma started to ascend toward the surface.

Emplacement occurred in a hypabyssal system such as in a dike or sill near the surface.

We also confirmed that NWA 10441 and NWA 12335 are enriched basaltic (diabasic) shergottites. NWA 10441 is very similar to its proposed pair NWA 8657 (Howarth et al., 2018), though definitive confirmation would require ejection (combined cosmic ray exposure and terrestrial age) and geochronological ages. The crystallization histories of NWA 10441 and NWA 12335 are slightly different. NWA 10441 represents multistage crystallization, where pyroxenes became entrained in an ascending basaltic magma. NWA 12335 represents continuous crystallization of pyroxenes until final extrusion. Both shergottites finally erupted onto the Martian surface as lavas, evidenced by the metastable Fs-pigeonite and pyroxferroite rims, which are only preserved during rapid cooling. These new shergottites add to the consistent story of basaltic shergottites erupting as lavas onto the surface and poikilitic shergottites being emplaced hypabyssally near the surface. Combining new methods such as HRXCT and EBSD with traditional methods, we can examine these rocks nondestructively in ever greater detail. We have demonstrated that the combination of these techniques can be very effective, and sometimes more suitable than destructive techniques, especially with regard to highly weathered samples.

Acknowledgments—We thank the reviewers for their detailed comments, which have significantly improved the manuscript. We thank the Institute for Meteoritics at the University of New Mexico for providing the materials used in this study. This research was undertaken using the Microscopy and Microscope Facility instrumentation (ARC LE130100051 and LE1409100150) at the John de Laeter Centre, Curtin University. Analysis in the John de Laeter Centre GeoHistory Facility was enabled by AuScope (auscope.org.au) and the Australian Government via the National Collaborative Research Infrastructure Strategy (NCRIS). The authors acknowledge the facilities, and the scientific and technical assistance of Microscopy Australia at the Centre for Microscopy, Characterisation & Analysis, the University of Western Australia, a facility funded by the University, State and Commonwealth Governments. This research was funded through the Australian Research Council grant FT170100024. Open access publishing facilitated by Curtin University, as part of the Wiley - Curtin University agreement via the Council of Australian University Librarians.

Data Availability Statement—The data that support the findings of this study will be openly available at the

Curtin University library depository. A doi will be supplied on acceptance of this article.

Editorial Handling—Prof. Alexander Ruzicka

REFERENCES

- Agee, C. B., Wilson, N. V., McCubbin, F. M., Ziegler, K., Polyak, V. J., Sharp, Z. D., Asmerom, Y. et al. 2013. Unique Meteorite from Early Amazonian Mars: Water-Rich Basaltic Breccia Northwest Africa 7034. *Science* 339: 780–5. <https://doi.org/10.1126/science.1228858>.
- Anand, M., James, S., Greenwood, R. C., Johnson, D., Franchi, I. A., and Grady, M. M. 2008. Mineralogy and Geochemistry of Shergottite RBT 04262 (Abstract #2173). 39th Lunar and Planetary Science Conference. CD-ROM.
- Artemieva, N., and Ivanov, B. 2004. Launch of Martian Meteorites in Oblique Impacts. *Icarus* 171: 84–101.
- Babadzhanov, P. B. 2002. Fragmentation and Densities of Meteoroids. *Astronomy & Astrophysics* 384: 317–21.
- Barrat, J. A., Gillet, P., Sautter, V., Jambon, A., Javoy, M., Göpel, C., Lesourd, M., Keller, F., and Petit, E. 2002. Petrology and Chemistry of the Basaltic Shergottite North West Africa 480. *Meteoritics & Planetary Science* 37: 487–99. <https://doi.org/10.1111/j.1945-5100.2002.tb00835.x>
- Barrat, J. A., Jambon, A., Bohn, M., Gillet, P., Sautter, V., Göpel, C., Lesourd, M., and Keller, F. 2002. Petrology and Chemistry of the Picritic Shergottite North West Africa 1068 (NWA 1068). *Geochimica et Cosmochimica Acta* 66: 3505–18. [https://doi.org/10.1016/s0016-7037\(02\)00934-1](https://doi.org/10.1016/s0016-7037(02)00934-1)
- Benoit, P. H., Sears, D. W. G., Akridge, J. M. C., Bland, P. A., Berry, F. J., and Pillinger, C. T. 2000. The Non-Trivial Problem of Meteorite Pairing. *Meteoritics & Planetary Science* 35: 393–417.
- Bland, P. A., Berry, F. J., Smith, T. B., Skinner, S. J., and Pillinger, C. T. 1996. The Flux of Meteorites to the Earth and Weathering in Hot Desert Ordinary Chondrite Finds. *Geochimica et Cosmochimica Acta* 60: 2053–9. [https://doi.org/10.1016/0016-7037\(96\)00125-1](https://doi.org/10.1016/0016-7037(96)00125-1)
- Borg, L. E., and Draper, D. S. 2003. A Petrogenetic Model for the Origin and Compositional Variation of the Martian Basaltic Meteorites. *Meteoritics & Planetary Science* 38: 1713–31.
- Bouvier, A., Gattacceca, J., Agee, C., Grossman, J., and Metzler, K. 2017. The Meteoritical Bulletin, No. 104. *Meteoritics & Planetary Science* 52: 2284.
- Bouvier, A., Gattacceca, J., Grossman, J., and Metzler, K. 2017. The Meteoritical Bulletin, No. 105. *Meteoritics & Planetary Science* 52: 2411.
- Bridges, J. C., and Warren, P. H. 2006. The SNC Meteorites: Basaltic Igneous Processes on Mars. *Journal of the Geological Society* 163: 229–51.
- Cao, T., He, Q., and Xue, Z. Q. 2018. Petrogenesis of Basaltic Shergottite NWA 8656. *Earth and Planetary Physics* 2: 384–97.
- Combs, L. M., Udry, A., Howarth, G. H., Richter, M., Lapen, T. J., Gross, J., Ross, D. K., Rahib, R. R., and Day, J. M. D. 2019. Petrology of the Enriched Poikilitic Shergottite Northwest Africa 10169: Insight into the Martian Interior. *Geochimica et Cosmochimica Acta* 266: 435–62.

- Cousin, A., Sautter, V., Payré, V., Forni, O., Mangold, N., Gasnault, O., Le Deit, L. et al. 2017. Classification of Igneous Rocks Analyzed by ChemCam at Gale Crater, Mars. *Icarus* 288: 265–83. <https://doi.org/10.1016/j.icarus.2017.01.014>.
- Crozaz, G., Floss, C., and Wadhwa, M. 2003. Chemical Alteration and REE Mobilization in Meteorites from Hot and Cold Deserts. *Geochimica et Cosmochimica Acta* 67: 4727–41.
- Crozaz, G., and Wadhwa, M. 2001. The Terrestrial Alteration of Saharan Shergottites Dar al Gani 476 and 489: A Case Study of Weathering in a Hot Desert Environment. *Geochimica et Cosmochimica Acta* 65: 971–7.
- El Goresy, A., Gillet, P. H., Miyahara, M., Ohtani, E., Ozawa, S., Beck, P., and Montagnac, G. 2013. Shock-Induced Deformation of Shergottites: Shock-Pressures and Perturbations of Magmatic Ages on Mars. *Geochimica et Cosmochimica Acta* 101: 233–62.
- Filiberto, J., Chin, E., Day, J. M. D., Franchi, I. A., Greenwood, R. C., Gross, J., Penniston-Dorland, S. C., Schwenzer, S. P., and Treiman, A. H. 2012. Geochemistry of Intermediate Olivine-Phyric Shergottite Northwest Africa 6234, with Similarities to Basaltic Shergottite Northwest Africa 480 and Olivine-Phyric Shergottite Northwest Africa 2990. *Meteoritics & Planetary Science* 47: 1256–73.
- Filiberto, J., Gross, J., Trela, J., and Ferré, E. C. 2014. Gabbroic Shergottite Northwest Africa 6963: An Intrusive Sample of Mars. *American Mineralogist* 99: 601–6.
- Filiberto, J., Gross, J., Udry, A., Trela, J., Wittmann, A., Cannon, K. M., Penniston-Dorland, S. et al. 2018. Shergottite Northwest Africa 6963: A Pyroxene-Cumulate Martian Gabbro. *Journal of Geophysical Research: Planets* 123: 1823–41.
- Filiberto, J., Musselwhite, D. S., Gross, J., Burgess, K., Le, L., and Treiman, A. H. 2010. Experimental Petrology, Crystallization History, and Parental Magma Characteristics of Olivine-Phyric Shergottite NWA 1068: Implications for the Petrogenesis of “Enriched” Olivine-Phyric Shergottites. *Meteoritics & Planetary Science* 45: 1258–70. <https://doi.org/10.1111/j.1945-5100.2010.01080.x>.
- Ford, R. L., Benedix, G. K., McCoy, T. J., and Rushmer, T. 2008. Partial Melting of H6 Ordinary Chondrite Kernouvé: Constraints on the Effects of Reducing Conditions on Oxidized Compositions. *Meteoritics & Planetary Science* 43: 1399–414.
- Forman, L. V., Timms, N. E., Bland, P. A., Daly, L., Benedix, G. K., and Trimby, P. W. 2019. A Morphologic and Crystallographic Comparison of CV Chondrite Matrices. *Meteoritics & Planetary Science* 54: 2633–51.
- Fritz, J., Artemieva, N., and Greshake, A. 2005. Ejection of Martian Meteorites. *Meteoritics & Planetary Science* 40: 1393–411.
- Gattacceca, J., Bouvier, A., Grossman, J., Metzler, K., and Uehara, M. 2019. The Meteoritical Bulletin, No. 106. *Meteoritics & Planetary Science* 54: 469–71.
- Gattacceca, J., McCubbin, F. M., Bouvier, A., and Grossman, J. 2020. The Meteoritical Bulletin, No. 107. *Meteoritics & Planetary Science* 55: 460–2.
- Godel, B. 2013. High-Resolution X-Ray Computed Tomography and Its Application to Ore Deposits: From Data Acquisition to Quantitative Three-Dimensional Measurements with Case Studies from Ni-Cu-PGE Deposits. *Economic Geology* 108: 2005–19.
- Goodrich, C. A., Herd, C. D. K., and Taylor, L. A. 2003. Spinel and Oxygen Fugacity in Olivine-Phyric and Lherzolitic Shergottites. *Meteoritics & Planetary Science* 38: 1773–92.
- Harvey, R. P., McCoy, T. J., and Leshin, L. A. 1996. Shergottite QUE94201: Texture, Mineral Compositions, and Comparison with Other Basaltic Shergottites (Abstract). 27th Lunar and Planetary Science Conference. p. 497.
- He, Q., Xiao, L., Balta, J. B., Baziotis, I. P., Hsu, W., and Guan, Y. 2015. Petrography and Geochemistry of the Enriched Basaltic Shergottite Northwest Africa 2975. *Meteoritics & Planetary Science* 50: 2024–44.
- Head, J. N., Melosh, H. J., and Ivanov, B. A. 2002. Martian Meteorite Launch: High-Speed Ejecta from Small Craters. *Science* 298: 1752–6.
- Herd, C. D. K., Walton, E. L., Agee, C. B., Muttik, N., Ziegler, K., Shearer, C. K., Bell, A. S. et al. 2017. The Northwest Africa 8159 Martian Meteorite: Expanding the Martian Sample Suite to the Early Amazonian. *Geochimica et Cosmochimica Acta* 218: 1–26.
- Howarth, G. H., Pernet-Fisher, J. F., Balta, J. B., Barry, P. H., Bodnar, R. J., and Taylor, L. A. 2014. Two-Stage Polybaric Formation of the New Enriched, Pyroxene-Oikocrystic, Lherzolitic Shergottite, NWA 7397. *Meteoritics & Planetary Science* 49: 1812–30.
- Howarth, G. H., Pernet-Fisher, J. F., Bodnar, R. J., and Taylor, L. A. 2015. Evidence for the Exsolution of Cl-Rich Fluids in Martian Magmas: Apatite Petrogenesis in the Enriched Lherzolitic Shergottite Northwest Africa 7755. *Geochimica et Cosmochimica Acta* 166: 234–48.
- Howarth, G. H., Udry, A., and Day, J. M. D. 2018. Petrogenesis of Basaltic Shergottite Northwest Africa 8657: Implications for fO_2 Correlations and Element Redistribution During Shock Melting in Shergottites. *Meteoritics & Planetary Science* 53: 249–67.
- Hui, H., Peslier, A. H., Lapen, T. J., Shafer, J. T., Brandon, A. D., and Irving, A. J. 2011. Petrogenesis of Basaltic Shergottite Northwest Africa 5298: Closed-System Crystallization of an Oxidized Mafic Melt. *Meteoritics & Planetary Science* 46: 1313–28.
- Ikeda, Y., Kimura, M., Takeda, H., Shimoda, G., Kita, N. T., Morishita, Y., Suzuki, A., Jagoutz, E., and Dreibus, G. 2006. Petrology of a New Basaltic Shergottite: Dhofar 378. *Antarctic Meteorite Research* 19: 20–44.
- Irving, A. J., Kuehner, S. M., Herd, C. D. K., Gellissen, M., Rumble, D., Lapan, T. J., Ralew, S., and Altmann, M. 2010. Olivine-Bearing Diabasic Shergottite Northwest Africa 5990: Petrology and Composition of a New Type of Depleted Martian Igneous Rock. 41st Lunar and Planetary Science Conference. CD-ROM.
- Jambon, A., Barrat, J. A., Sautter, V., Gillet, P. H., Göpel, C., Javoy, M., Joron, J. L., and Lesourd, M. 2002. The Basaltic Shergottite Northwest Africa 856: Petrology and Chemistry. *Meteoritics & Planetary Science* 37: 1147–64.
- Kizovski, T. V., Tait, K. T., Cecco, V. E. D., White, L. F., and Moser, D. E. 2019. Detailed Mineralogy and Petrology of Highly Shocked Poikilitic Shergottite Northwest Africa 6342. *Meteoritics & Planetary Science* 54: 768–84.
- Kring, D. A., Gleason, J. D., Swindle, T. D., Nishiizumi, K., Caffee, M. W., Hill, D. H., Jull, A. J. T., and Boynton, W. V. 2003. Composition of the First Bulk Melt Sample from a canic Region of Mars: Queen Alexandra Range 94201. *Meteoritics & Planetary Science* 38: 1833–48.
- Lin, Y., Guan, Y., Wang, D., Kimura, M., and Leshin, L. A. 2005. Petrogenesis of the New Lherzolitic Shergottite

- Grove Mountains 99027: Constraints of Petrography, Mineral Chemistry, and Rare Earth Elements. *Meteoritics & Planetary Science* 40: 1599–619.
- Lin, Y., Hu, S., Miao, B., Xu, L., Liu, Y., Xie, L., Feng, L., and Yang, J. 2013. Grove Mountains 020090 Enriched Lherzolithic Shergottite: A Two-Stage Formation Model. *Meteoritics & Planetary Science* 48: 1572–89.
- Lindsley, D. H., and Burnham, C. W. 1970. Pyroxferroite: Stability and X-Ray Crystallography of Synthetic $\text{Ca}_{0.15}\text{Fe}_{0.85}\text{SiO}_3$ Pyroxenoid. *Science* 168: 364–7.
- Liu, Y., Floss, C., Day, J. M. D., Hill, E., and Taylor, L. A. 2009. Petrogenesis of Lunar Mare Basalt Meteorite Miller Range 05035. *Meteoritics & Planetary Science* 44: 261–84.
- Llorca, J., Roszjar, J., Cartwright, J. A., Bischoff, A., Ott, U., Pack, A., Merchel, S. et al. 2013. The Ksar Ghilane 002 Shergottite—The 100th Registered Martian Meteorite Fragment. *Meteoritics & Planetary Science* 48: 493–513.
- Lodders, K. 1998. A Survey of Shergottite, Nakhilite and Chassigny Meteorites Whole-Rock Compositions. *Meteoritics & Planetary Science* 33: A183–90. <https://doi.org/10.1111/j.1945-5100.1998.tb01331.x>.
- Lodders, K., and Fegley Jr., B. 1998. *The Planetary Scientist's Companion*. New York: Oxford University Press.
- McCoy, T. J., Taylor, G. J., and Keil, K. 1992. Zagami: Product of a Two-Stage Magmatic History. *Geochimica et Cosmochimica Acta* 56: 3571–82.
- McCubbin, F. M., Elardo, S. M., Shearer, C. K., Smirnov, A., Hauri, E. H., and Draper, D. S. 2013. A Petrogenetic Model for the Comagmatic Origin of Chassignites and Nakhilites: Inferences from Chlorine-Rich Minerals, Petrology, and Geochemistry. *Meteoritics & Planetary Science* 48: 819–53.
- McSween, H. Y. 2015. Petrology on Mars. *American Mineralogist* 100: 2380–95.
- McSween, H. Y., Eisenhour, D. D., Taylor, L. A., Wadhwa, M., and Crozaz, G. 1996. QUE 94201 Shergottite: Crystallization of a Martian Basaltic Magma. *Geochimica et Cosmochimica Acta* 60: 4563–9.
- McSween, H. Y., and McLennan, S. M. 2013. Mars. In *Treatise on Geochemistry*, 2nd ed., edited by H. D. Holland and Karl K. Turekian, vol. 2, 251–300. Elsevier Inc. <https://doi.org/10.1016/B978-0-08-095975-7.00125-X>
- McSween, H. Y., and Treiman, A. H. 1998. Martian meteorites. In *Planetary Materials*, edited by J. J. Papike, 6–1–6–53. Reviews in Mineralogy, vol. 36. Washington, D.C.: Mineralogical Society of America.
- Mikouchi, T., and Barrat, J. A. 2009. NWA 5029 Basaltic Shergottites: A Clone of NWA 480/1460? *Meteoritics & Planetary Science Supplement* 72: 5344.
- Mikouchi, T., Miyamoto, M., and McKay, G. A. 1998. Mineralogy of Antarctic Basaltic Shergottite Queen Alexandra Range 94201: Similarities to Elephant Moraine A79001 (Lithology B) Martian Meteorite. *Meteoritics & Planetary Science* 33: 181–9.
- Mikouchi, T., Miyamoto, M., and McKay, G. A. 2001. Mineralogy and Petrology of the Dar al Gani 476 Martian Meteorite: Implications for its Cooling History and Relationship to Other Shergottites. *Meteoritics & Planetary Science* 36: 531–48.
- Paton, C., Hellstrom, J., Paul, B., Woodhead, J., and Hergt, J. 2011. Iolite: Freeware for the Visualisation and Processing of Mass Spectrometric Data. *Journal of Analytical Atomic Spectrometry* 26: 2508–18.
- Rae, A. S. P., Collins, G. S., Morgan, J. V., Salge, T., Christeson, G. L., Leung, J., Lofi, J. et al. 2019. Impact-Induced Porosity and Microfracturing at the Chicxulub Impact Structure. *Journal of Geophysical Research: Planets* 124: 1960–78.
- Rahib, R. R., Udry, A., Howarth, G. H., Gross, J., Paquet, M., Combs, L. M., Laczniak, D. L., and Day, J. M. D. 2019. Mantle Source to Near-Surface Emplacement of Enriched and Intermediate Poikilitic Shergottites in Mars. *Geochimica et Cosmochimica Acta* 266: 463–96.
- Riches, A. J. V., Liu, Y., Day, J. M. D., Puchtel, I. S., Rumble, D., McSween, H. Y., Walker, R. J., and Taylor, L. A. 2011. Petrology and Geochemistry of Yamato 984028: A Cumulate Lherzolithic Shergottite with Affinities to Y 000027, Y 000047, and Y 000097. *Polar Science* 4: 497–514.
- Roszjar, J., Bischoff, A., Llorca, J., and Pack, A. 2012. Ksar Ghilane 002 (KG 002)—A New Shergottite: Discovery, Mineralogy, Chemistry and Oxygen Isotopes (Abstract #1780). 43rd Lunar and Planetary Science Conference. CD-ROM.
- Rubin, A. E., Warren, P. H., Greenwood, J. P., Verish, R. S., Leshin, L. A., Hervig, R. L., Clayton, R. N., and Mayeda, T. K. 2000. Los Angeles: The Most Differentiated Basaltic Martian Meteorite. *Geology* 28: 1011–4.
- Sautter, V., Toplis, M. J., Wiens, R. C., Cousin, A., Fabre, C., Gasnault, O., Maurice, S. et al. 2015. In Situ Evidence for Continental Crust on Early Mars. *Nature Geoscience* 8: 605–9. <https://doi.org/10.1038/ngeo2474>.
- Sharp, T. G., and DeCarli, P. S. 2006. Shock Effects in Meteorites. In *Meteorites and the Early Solar System II*, edited by D. S. Lauretta, and H. Y. McSween Jr., 653–77. Tucson, Arizona: University of Arizona Press.
- Stöffler, D. 1984. Glasses Formed by Hypervelocity Impact. *Journal of Non-Crystalline Solids* 67: 465–502.
- Stöffler, D., Hamann, C., and Metzler, K. 2018. Shock Metamorphism of Planetary Silicate Rocks and Sediments: Proposal for an Updated Classification System. *Meteoritics & Planetary Science* 53: 5–49.
- Stöffler, D., Ostertag, R., Jammes, C., Pfannschmidt, G., Gupta, P. R., Simon, S. B., Papike, J. J., and Beauchamp, R. H. 1986. Shock Metamorphism and Petrography of the Shergotty Achondrite. *Geochimica et Cosmochimica Acta* 50: 889–903.
- Treiman, A. H., and Filiberto, J. 2015. Geochemical Diversity of Shergottite Basalts: Mixing and Fractionation, and Their Relation to Mars Surface Basalts. *Meteoritics & Planetary Science* 50: 632–48.
- Treiman, A. H., McKay, G. A., Bogard, D. D., Mittlefehldt, D. W., Wang, M. S., Keller, L., Lipschutz, M. E., Lindstrom, M. M., and Garrison, D. 1994. Comparison of the LEW 88516 and ALHA77005 Martian Meteorites: Similar but Distinct. *Meteoritics* 29: 581–92.
- Udry, A., Howarth, G. H., Herd, C. D. K., Day, J. M. D., Lapen, T. J., and Filiberto, J. 2020. What Martian Meteorites Reveal About the Interior and Surface of Mars. *Journal of Geophysical Research: Planets* 125. <https://doi.org/10.1029/2020je006523>.
- Udry, A., Howarth, G. H., Lapen, T. J., and Righter, M. 2017. Petrogenesis of the NWA 7320 Enriched Martian Gabbroic Shergottite: Insight into the Martian Crust. *Geochimica et Cosmochimica Acta* 204: 1–18.
- Usui, T., McSween, H. Y., and Floss, C. 2008. Petrogenesis of Olivine-Phyric Shergottite Yamato 980459, Revisited. *Geochimica et Cosmochimica Acta* 72: 1711–30.

- Usui, T., Sanborn, M., Wadhwa, M., and McSween, H. Y. 2010. Petrology and Trace Element Geochemistry of Robert Massif 04261 and 04262 Meteorites, the First Examples of Geochemically Enriched Lherzolithic Shergottites. *Geochimica et Cosmochimica Acta* 74: 7283–306.
- Walton, E. L., Irving, A. J., Bunch, T. E., and Herd, C. D. K. 2012. Northwest Africa 4797: A Strongly Shocked Ultramafic Poikilitic Shergottite Related to Compositionally Intermediate Martian Meteorites. *Meteoritics & Planetary Science* 47: 1449–74.
- Walton, E. L., and Spray, J. G. 2003. Mineralogy, Microtexture, and Composition of Shock-Induced Melt Pockets in the Los Angeles Basaltic Shergottite. *Meteoritics & Planetary Science* 38: 1865–75.
- Warren, P. H., Greenwood, J. P., and Rubin, A. E. 2004. Los Angeles: A Tale of Two Stones. *Meteoritics & Planetary Science* 39: 137–56.
- Wittke, J. H., Bunch, T. E., Irving, A. J., Farmer, M., and Strope, J. 2006. Northwest Africa 2975: An Evolved Basaltic Shergottite with Vesicular Glass Pockets and Trapped Melt Inclusions (Abstract #1368). 37th Lunar and Planetary Science Conference. CD-ROM.
- Xirouchakis, D., Draper, D. S., Schwandt, C. S., and Lanzarotti, A. 2002. Crystallization Conditions of Los Angeles, a Basaltic Martian Meteorite. *Geochimica et Cosmochimica Acta* 66: 1867–80.
- Zipfel, J., Schröder, C., Jolliff, B. L., Gellert, R., Herkenhoff, K. E., Rieder, R., Anderson, R. et al. 2011. Bounce Rock—A Shergottite-Like Basalt Encountered at Meridiani Planum, Mars. *Meteoritics & Planetary Science* 46: 1–20. <https://doi.org/10.1111/j.1945-5100.2010.01127.x>.
-